This article has been accepted for publication in a future issue of this journal, but has not been fully edited. Content may change prior to final publication. Citation information: DOI 10.1109/TPEL.2014.2369573, IEEE Transactions on Power Electronics

Systematic Derivation of a Family of Output-Impedance Shaping Methods for Power Converters – A Case Study Using Fuel Cell-Battery-Powered Single-Phase Inverter System

Lingling Cao, K. H. Loo, Y. M. Lai *

Abstract

For power converters used in renewable energy systems, output-impedance design has become an important design consideration for minimizing the impacts of low-frequency harmonic current on the lifetime of ripple-sensitive energy sources such as fuel cells and photovoltaic cells. In the literature various methods are proposed to tackle this design issue but they are frequently treated in isolation from each other and specific to the systems being discussed. In this paper, a systematic derivation of four basic modes of output-impedance shaping method is presented. These basic modes can be directly inferred from the Mason's gain formula and other methods are in essence derivatives or combinations of these basic modes. By using a fuel-cell-battery-powered single-phase inverter as an implementation example, their characteristics are discussed thoroughly and their performances in shaping converter's output impedance are evaluated experimentally.

1 Introduction

In many renewable energy systems involving ripple-sensitive energy sources such as fuel cells and photovoltaic cells, the presence of low-frequency ac component at around 100 Hz in their output current can have significant detrimental effects on the lifetime of these devices when they are used to drive inverter load [1]–[4]. For this reason, output-impedance design of the converter(s) forming these energy systems has become an important consideration with the aim to prevent the low-frequency ac current from being drawn from these energy sources.

*The authors are with The Department of Electronic and Information Engineering, The Hong Kong Polytechnic University, Hong Kong Tel: (852) 2766 4744 Fax: (852) 2362 8439 Email: lingling.cao@connect.polyu.hk.

This article has been accepted for publication in a future issue of this journal, but has not been fully edited. Content may change prior to final publication. Citation information: DOI 10.1109/TPEL.2014.2369573, IEEE Transactions on Power Electronics

There are in general two categories of methods being adopted for achieving this aim. The first category of methods involves increasing the output impedance of the converter associated with the ripple-sensitive energy source [5]–[10]. If there is no other energy storage present in the system, the low-frequency ac current will typically be drawn from the dc-link capacitor and, as a result, increasing the amplitude of the voltage ripple on the dc bus voltage. The inverter's operation can be adversely affected when the amplitude of the voltage ripple becomes excessively large, unless a very large dc-link capacitor is used to minimize the voltage ripple. In addition, the frequent periodic charging and discharging of the dc-link capacitor, typically of electrolytic type, will also reduce its lifetime due to internal heating. If, on the other hand, a dedicated energy storage, battery or super-capacitor bank, is present and connected in parallel to the dc bus, decreasing the output impedance of the converter associated with the energy storage, as a second category of methods, can create a low-impedance path for the flow of the low-frequency ac current and prevent it from being drawn from either the ripple-sensitive energy source or the dc-link capacitor [11]–[16]. The use of dedicated energy storage is advantageous in terms of meeting transient load changes, such as offering a substantially increased peak power capability and the ability to absorb power from energy-regenerative loads, while, with properly designed output impedance, assisting in preserving the lifetimes of both the energy source and the dc-link capacitor.

Leaving aside the practical impacts of these two categories of methods, it should be clear that they indeed have the same origin in the design of converter's output impedance, with one focusing on the energy source branch and the other on the energy storage branch. In this paper, efforts are made to systematically analyze and explore the various fundamental approaches to affecting, or technically, shaping the output impedance of converters in general, when they are used in renewable energy systems or other power electronic systems encountering similar design issue. The analysis to be presented here is founded on the Mason's gain formula, from which two fundamental ideas are derived. The first idea suggests the addition of forward paths for minimizing the numerator of the Mason's gain formula, and the second one suggests the addition of feedback loops for maximizing the denominator. Collectively these ideas give rise to four basic modes of output-impedance shaping method, namely the load-current feed-forward, virtual-resistor, virtual-capacitor, and virtual-inductor approach. These methods had been discussed in literature in different ways for different applications but they were often treated individually and in isolation from each other [17]–[26]. It will be shown that all of them can be directly inferred from the Mason's gain formula by inspection.

In this paper, these ideas will be developed systematically and discussed thoroughly, and demonstrated by using a fuel-cell-battery-powered single-phase inverter as an implementation example, in which case the fuel cell represents the ripple-sensitive energy source and the battery represents the dedicated energy storage. A two-

This article has been accepted for publication in a future issue of this journal, but has not been fully edited. Content may change prior to final publication. Citation information: DOI 10.1109/TPEL.2014.2369573, IEEE Transactions on Power Electronics

input bidirectional dual active bridge (DAB) dc-dc converter is adopted for interfacing the fuel cell and battery to the inverter load due to its high efficiency and flexible power-flow control. All four basic modes of the output-impedance shaping method will be implemented on the converter and their characteristics and performances evaluated experimentally. With reference to the presented example, the same methods and their derivatives (combination of the four basic modes) can be broadly applied to other converters subject to application-specific output-impedance requirements.

This paper is organized as follows. Section 2 presents a brief review of the multi-input bidirectional DAB dc-dc converter, and a simplified model of the converter is derived. This is followed by a systematic derivation of the four basic modes of output-impedance shaping method from the Mason's gain formula in Section 3, during which the idea of forward-path-gain compensation is also introduced as a way to reshape the converter's dynamic response in the presence of output-impedance shaping. Section 4 discusses the design and practical implementation of these four basic modes of output-impedance shaping, and experimental results including both static and dynamic characteristics and FFT analysis of the main converter's waveforms are presented in Section 5. Finally, the work is concluded in Section 6.

2 Bidirectional Dual Active Bridge DC-DC Converter

2.1 Multi-Input Bi-Directional Dual Active Bridge DC-DC Converter

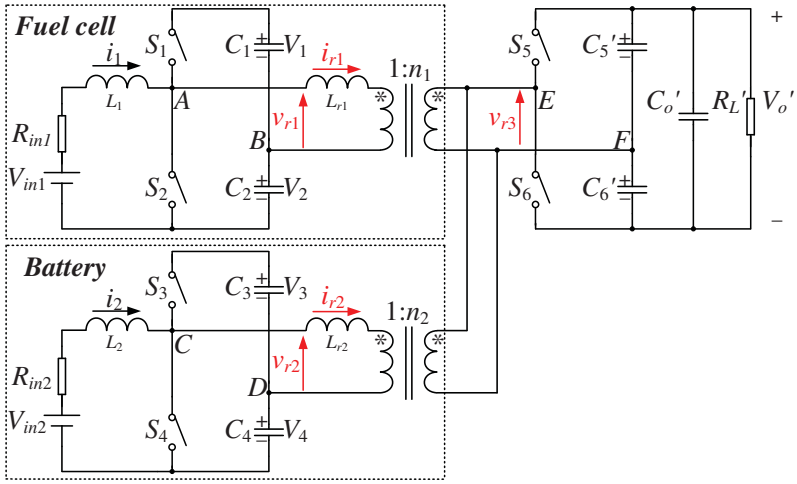

Figure 1: Multi-input bidirectional DAB dc-dc converter with shared secondary half-bridge cell.

Bidirectional dual active bridge (DAB) dc-dc converters [27] are widely used in renewable-energy-based power conditioning systems due to several advantages such as flexible power flow control, realization of zero-

This article has been accepted for publication in a future issue of this journal, but has not been fully edited. Content may change prior to final publication. Citation information: DOI 10.1109/TPEL.2014.2369573, IEEE Transactions on Power Electronics

voltage switching, and high efficiency. In this work, the topology is adapted for multi-input operation [28], and the resulting converter is shown in Fig. 1. The multi-input bidirectional DAB dc-dc converter developed here uses two separate transformers for the input half-bridge cells so that each of the input half-bridge cells can be controlled independently, thus enabling a more versatile implementation of various power-flow control strategies. By using phase-shift control, the bidirectional power flow of each of the input half-bridge cells can be controlled by adjusting the phase difference between the transformer's primary and secondary voltages.

With reference to Fig. 1, $v_{r1} \sim v_{r2}$, and v_{r3} represents the output voltages of the two input half-bridge cells and the shared secondary half-bridge cell, respectively. The capacitors $C_1 \sim C_4$ and $C_5' \sim C_6'$ are assumed to be sufficiently large that the voltages $V_1 \sim V_4$ and $V_5' \sim V_6'$ are reasonably assumed to be constant. The current flowing through the transformer's leakage inductance of input half-bridge cell 1 and 2 is denoted by i_{r1} and i_{r2}, respectively. By using phase-shift control, the power flow of each input half-bridge cells can be controlled by adjusting the phase difference (φ_1 or φ_2) between the transformer's primary and secondary voltages. According to the control strategies discussed above, the fuel cell branch always delivers power by controlling φ_1 larger than zero, while the energy storage branch can deliver power, absorb power, or have no contribution to the load by controlling the value of φ_2. For the two-input converter shown in Fig. 1, the power delivered by the fuel cell and energy storage, and the total power delivered by both, is given by Equation (1), (2), and (3), respectively.

$$P_f = \frac{\int_0^{2\pi} i_{r1}(\theta) v_{r1}(\theta)\, d\theta}{2\pi} = \frac{\varphi_1 \left(\pi - |\varphi_1|\right)}{4\pi L_{r1}\omega} \frac{V_{12} V_{56}'}{n_1} \tag{1}$$

$$P_b = \frac{\int_0^{2\pi} i_{r2}(\theta) v_{r2}(\theta)\, d\theta}{2\pi} = \frac{\varphi_2 \left(\pi - |\varphi_2|\right)}{4\pi L_{r2}\omega} \frac{V_{34} V_{56}'}{n_2} \tag{2}$$

$$P_o = P_f + P_b \tag{3}$$

where $V_{12} = (V_1 + V_2)$, $V_{34} = (V_3 + V_4)$, and $V_{56}' = (V_5' + V_6') = V_o'$. By imposing the condition $\varphi_1 > 0$, the fuel cell branch always delivers power to the load or energy storage, while the energy storage branch can be controlled to deliver power ($\varphi_2 > 0$), absorb power ($\varphi_2 < 0$), or become inactive ($\varphi_2 = 0$).

2.2 Output Impedance of Energy Storage Branch

Since the two-input bidirectional DAB dc-dc converter shown in Fig. 1 is effectively two single-input converters connected in parallel, each of them will exhibit the same small-signal characteristics. When the parallel-connected converters are used to drive an inverter load, the resulting low-frequency harmonic current will mainly

This article has been accepted for publication in a future issue of this journal, but has not been fully edited. Content may change prior to final publication. Citation information: DOI 10.1109/TPEL.2014.2369573, IEEE Transactions on Power Electronics

flow from the energy storage, and therefore the output impedance of the energy storage branch is of greater interest and will be analyzed in more detail.

As given by Equation (2), the power flow of the energy storage branch can be described by the following equation.

$$P_b = \frac{V_{in2} V_o}{2\pi\omega L_{r2}} \varphi(\pi - |\varphi|) \tag{4}$$

where L_{r2} is the transformer's leakage inductance, V_o is the output voltage reflected to the transformer's primary side, and φ is the phase difference between the transformer's primary and secondary voltages. Assuming that the voltage ripple on the dc bus voltage is small, that is, V_o is approximately constant, the converter's output current can be approximated by the following equation.

$$I_b = \frac{V_{in2}}{2\pi\omega L_{r2}} \varphi(\pi - |\varphi|) \tag{5}$$

Linearizing Equation (5) gives the small-signal transfer function from the phase difference $\tilde{\varphi}$ to the converter's output current $\tilde{i}_b$ as

$$\frac{\tilde{i}_b}{\tilde{\varphi}} = \frac{V_{in2}}{2\pi\omega L_{r2}} (\pi - 2|\varphi|) = G_{i\varphi} \tag{6}$$

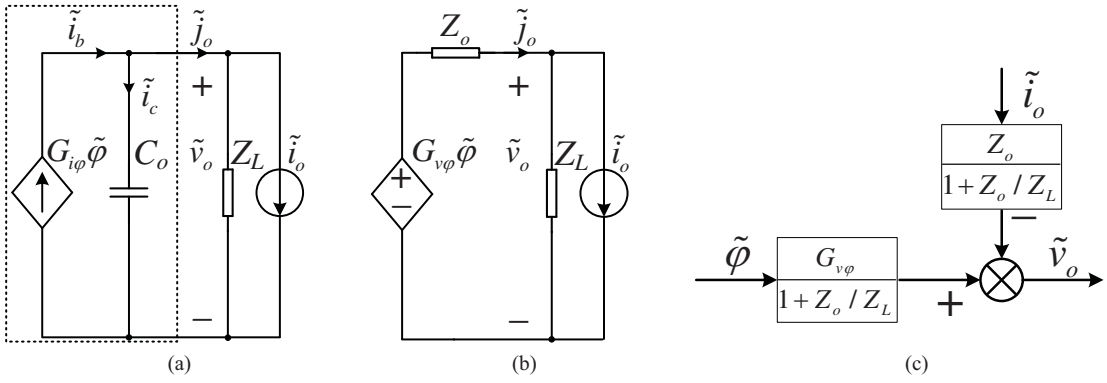

Figure 2: Approximate small-signal model of bidirectional DAB converter: (a) Norton equivalent circuit, (b) Thevenin equivalent circuit, and (c) transfer-function representation.

With the transfer function $G_{i\varphi}$ derived above, the converter can be modeled as shown in Fig. 2a, where C_o is the output capacitor and Z_L is the nominal load, both reflected to the transformer's primary side, and $\tilde{i}_o$ represents the perturbation in load current. By Thevenin's theorem, the converter can be modeled as a dependent

This article has been accepted for publication in a future issue of this journal, but has not been fully edited. Content may change prior to final publication. Citation information: DOI 10.1109/TPEL.2014.2369573, IEEE Transactions on Power Electronics

current source (Fig. 2a) or a dependent voltage source (Fig. 2b) by using the following transformation.

$$G_{v\varphi} = G_{i\varphi} Z_o \tag{7}$$

where

$$Z_o = \frac{1}{sC_o} \tag{8}$$

From Fig. 2b, the converter's small-signal output voltage $\tilde{v}_o$ can be derived as a function of $\tilde{\varphi}$ and $\tilde{i}_o$ after eliminating $\tilde{j}_o$.

$$\begin{aligned} \tilde{v}_o &= G_{v\varphi}\tilde{\varphi} - Z_o\tilde{j}_o \\ &= G'_{v\varphi}\tilde{\varphi} - Z'_o\tilde{i}_o \\ G'_{v\varphi} &= \frac{G_{v\varphi}}{1 + Z_o/Z_L} \\ Z'_o &= \frac{Z_o}{1 + Z_o/Z_L} \end{aligned} \tag{9}$$

The last equation provides a convenient tool for modeling the converter using transfer functions only; the resulting model is shown in Fig. 2c. Based on this model, the proposed control strategies can be clearly illustrated in the subsequent discussions. Before proceeding further, the approximate small-signal transfer functions $G'_{v\varphi}$ and Z'_o are verified against the exact transfer functions derived more rigorously in [28], with the converter's component values given in Table 1. From Fig. 3, it can be seen that the gain and phase plots of the approximate and exact transfer functions of $G'_{v\varphi}$ overlap with each other, except at the frequencies associated with the RHP zeros and poles on the imaginary axis which are not reproduced by the approximate transfer function. The effects of these differences can be minimized or even neglected as the converter's closed-loop bandwidth is typically designed to be well below these frequencies. The gain and phase plots of the approximate and exact transfer functions of Z'_o exhibit no noticeable difference and thus are not shown here.

This article has been accepted for publication in a future issue of this journal, but has not been fully edited. Content may change prior to final publication. Citation information: DOI 10.1109/TPEL.2014.2369573, IEEE Transactions on Power Electronics

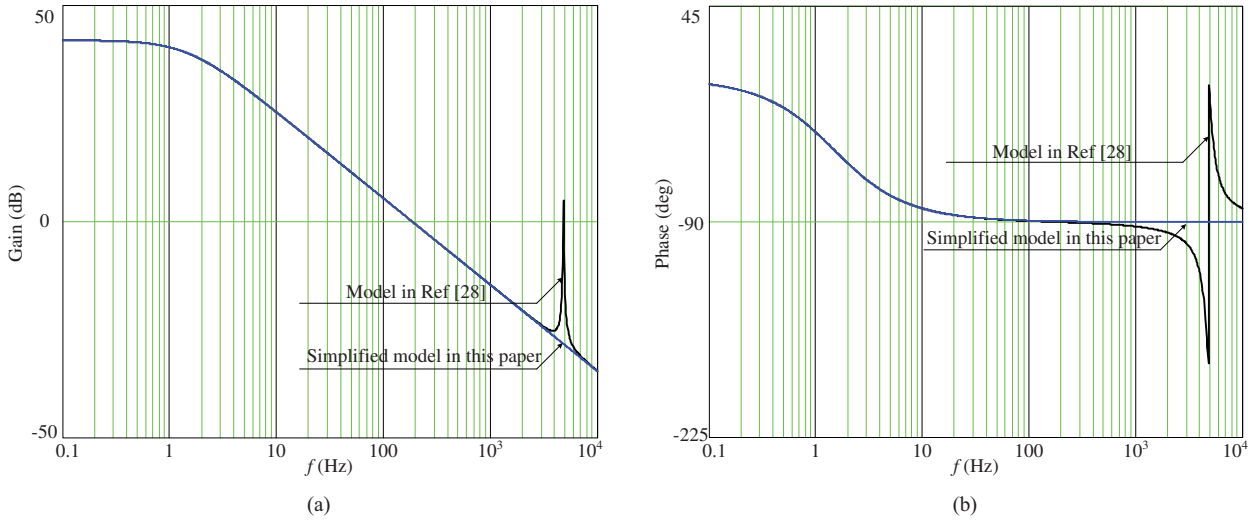

Figure 3: Bode plots of the phase-shift-to-output-voltage transfer function $G'_{v\varphi} = G_{v\varphi}/\left(1 + Z_o/Z_L\right)$.

3 Systematic Derivation of Output-Impedance Shaping Methods from Mason's Rule

In this section, the reduction of energy storage branch's output impedance is discussed based on the converter model derived in Section 2. As can be inferred from the well-known Mason's gain formula, introducing feed-forward and feedback paths to the converter's control system can contribute to the reduction of converter's closed-loop output impedance. In total, four different control approaches are proposed and discussed, one of which is based on feed-forward mechanism and three are based on feedback mechanism. For generality, all three modes of the feedback mechanism are discussed, although, as will be shown, their effectiveness can vary considerably from one to another.

3.1 Mason's Gain Formula

In a converter system containing one or more loops, its closed-loop output impedance Z_o^c can be generally described by the well-known Mason's gain formula [29].

$$Z_o^c = \frac{\tilde{v}_o}{-\tilde{i}_o} = \frac{\sum_{k=1}^{N} G_k \Delta_k}{\Delta} \tag{10}$$

$$\Delta = 1 - \sum L_i + \sum L_i L_j - \sum L_i L_j L_k + ... + (-1)^m \sum ... + ... \tag{11}$$

This article has been accepted for publication in a future issue of this journal, but has not been fully edited. Content may change prior to final publication. Citation information: DOI 10.1109/TPEL.2014.2369573, IEEE Transactions on Power Electronics

where N is the total number of forward paths from $\tilde{i}_o$ to $\tilde{v}_o$, G_k is the gain of the kth forward path, Δ_k is the cofactor value of Δ for the kth forward path, with the loops touching the kth forward path removed, L_i is the loop gain of the ith loop, L_iL_j is the product of the loop gains of any two non-touching loops.

It can be inferred from Equation (10) that the effective output impedance of the converter can be reduced by introducing additional paths into its control system if the additional paths are inserted in such a way that the numerator and denominator of the Mason's gain formula is decreased and increased, respectively. Specifically, as the numerator represents a summation of forward-path-gain-cofactor products ($\sum_{k=1}^{N} G_k\Delta_k$), the additional paths should be inserted in such a way that the newly introduced $G_k\Delta_k$ terms should partially or completely cancel the ones resulted from the existing forward paths. For the denominator, the opposite rule applies and requires that the individual terms in the summation reinforce each other for maximizing the denominator value. Note that in order to do so the constituent terms in Δ preceded by -1 should be made positive by introducing additional paths having appropriate signs.

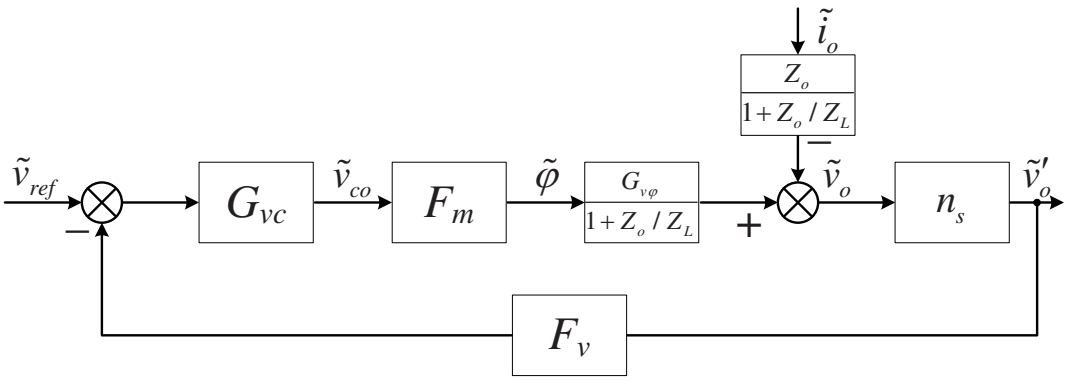

Figure 4: Basic control system of the converter used in the energy storage branch.

The basic control system of the bidirectional DAB dc-dc converter in the energy storage branch is shown in Fig. 4, where n_s is the transformer's turn ratio, F_v is the sampling gain, $\tilde{v}_{ref}$ is the reference signal for the dc bus voltage, G_{vc} is the compensation network's gain, $\tilde{v}_{co}$ is the control signal, and F_m is the modulator's gain. The system can be visualized as having two inputs, $\tilde{v}_{ref}$ and $\tilde{i}_o$, and one output $\tilde{v}_o$. Each of the two inputs has its own forward path to the output, but in respect of the converter's output impedance, which is the main subject of discussion, only the forward path from $\tilde{i}_o$ to $\tilde{v}_o$ is considered when minimizing the numerator of Equation (10). Besides, since the energy storage branch is required to provide dc bus voltage regulation, there must be at least one feedback path from $\tilde{v}_o$ for achieving this objective through the adjustment of the converter's control variable $\tilde{\varphi}$. It can be seen that introducing more feedback paths to the control system affects the denominator of Equation (10) only. The following discussions are based on extensions of this basic control

This article has been accepted for publication in a future issue of this journal, but has not been fully edited. Content may change prior to final publication. Citation information: DOI 10.1109/TPEL.2014.2369573, IEEE Transactions on Power Electronics

system. For reference, the output voltage $\tilde{v}_o$ produced by the closed-loop system is given by Equation (12), where L is the loop gain.

$$\begin{aligned} \tilde{v}_o &= \frac{G_{vc}F_m\frac{G_{v\varphi}}{1+Z_o/Z_L}}{1+L}\tilde{v}_{ref} - \frac{\frac{Z_o}{1+Z_o/Z_L}}{1+L}\tilde{i}_o \\ L &= G_{vc}F_mF_vn_s\frac{G_{v\varphi}}{1+Z_o/Z_L} \end{aligned} \tag{12}$$

3.2 Load-Current Feed-Forward

From the basic control system shown in Fig. 4, one existing forward path from $\tilde{i}_o$ to $\tilde{v}_o$ can be identified as $-Z_o/(1+Z_o/Z_L)$. According to the Mason's gain formula, the overall gain from $\tilde{i}_o$ to $\tilde{v}_o$ can be reduced, or ideally nullified, if one or more additional forward paths of opposite sign to the existing forward path are introduced into the control system. For clarity, the idea is illustrated by the addition of one forward path from $\tilde{i}_o$ to $\tilde{v}_o$.

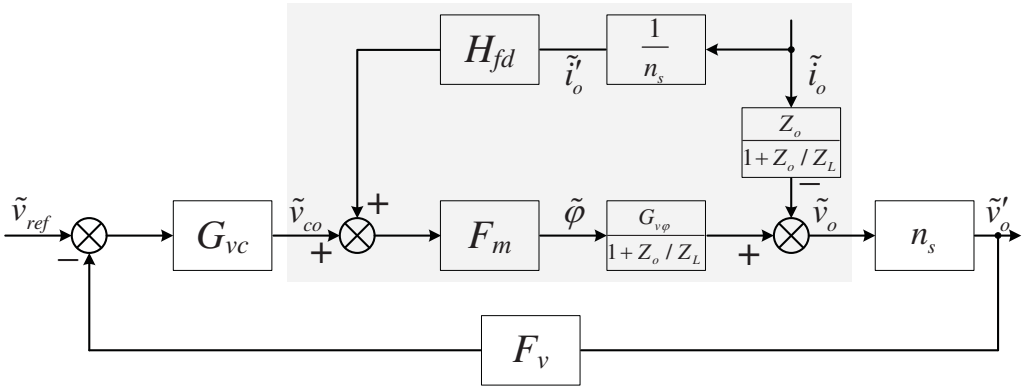

Figure 5: Additional forward path created by load-current feed-forward.

The additional forward path is created by feed-forwarding the load current $\tilde{i}_o$ and adding it to the control signal $\tilde{v}_{co}$. The feed-forward gain is denoted by H_{fd}. The transformer's turn ratio n_s is used to reflect both the output voltage $\tilde{v}_o$ and load current $\tilde{i}_o$ to the transformer's secondary side from where they are typically sampled. With the additional forward path, the output voltage $\tilde{v}_o$ produced by the closed-loop system is given by Equation (13), where L is the loop gain.

This article has been accepted for publication in a future issue of this journal, but has not been fully edited. Content may change prior to final publication. Citation information: DOI 10.1109/TPEL.2014.2369573, IEEE Transactions on Power Electronics

$$\begin{aligned} \tilde{v}_o &= \frac{G_{vc}F_m\frac{G_{v\varphi}}{1+Z_o/Z_L}}{1+L}\tilde{v}_{ref} - \frac{\left(\frac{Z_o}{1+Z_o/Z_L} - H_{fd}F_m\frac{1}{n_s}\frac{G_{v\varphi}}{1+Z_o/Z_L}\right)}{1+L}\tilde{i}_o \\ L &= G_{vc}F_mF_vn_s\frac{G_{v\varphi}}{1+Z_o/Z_L} \end{aligned} \tag{13}$$

By comparing Equation (13) to Equation (12), it can be seen that the converter's closed-loop output impedance $\tilde{v}_o/-\tilde{i}_o$ has been reduced by an amount proportional to the feed-forward gain H_{fd} with its closed-loop stability and dynamic response $\tilde{v}_o/\tilde{v}_{ref}$ remain unaffected. It can be further deduced that the closed-loop output impedance can be ideally reduced to zero if the following condition is satisfied and $H_{fd} = H_{fd0}$ is chosen.

$$\frac{Z_o}{1+Z_o/Z_L} - H_{fd0}F_m\frac{1}{n_s}\frac{G_{v\varphi}}{1+Z_o/Z_L} = 0 \implies H_{fd0} = \frac{Z_o}{G_{v\varphi}F_m}n_s = \frac{n_s}{G_{i\varphi}F_m} \tag{14}$$

Fig. 6 shows the plots of the open-loop and closed-loop output impedance of the converter with and without load-current feed-forward. It can be seen that both the open-loop and closed-loop output impedance at 100 Hz are significantly attenuated by feed-forwarding the load current to the control system, and the degree of attenuation improves as the feed-forward gain increases towards $H_{fd}/H_{fd0} = 1$, in agreement with the theoretical analysis presented above.

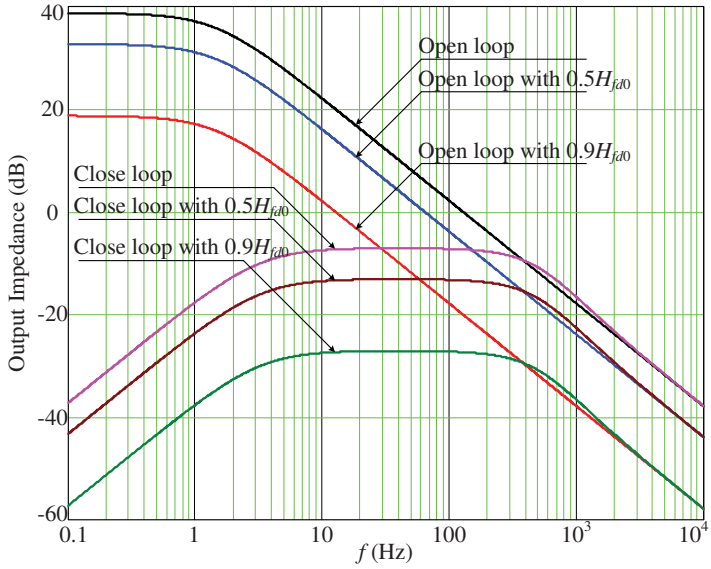

Figure 6: Open-loop and closed-loop output impedance with and without load-current feed-forward.

This article has been accepted for publication in a future issue of this journal, but has not been fully edited. Content may change prior to final publication. Citation information: DOI 10.1109/TPEL.2014.2369573, IEEE Transactions on Power Electronics

3.3 Output-Voltage Feedback

According to the Mason's gain formula, the overall gain from $\tilde{i}_o$ to $\tilde{v}_o$ can be reduced if one or more additional loops are introduced to the control system in such a way that they contribute positively to the denominator Δ. From the basic control system shown in Fig. 4, one existing negative feedback loop from $\tilde{v}_o$ to $\tilde{v}_{ref}$ can be identified with a feedback gain of $n_s F_v$. Since the existence of non-touching loops cannot be visualized for the system shown in Fig. 4, all additional loops must constitute negative feedback loops according to Equation (11) so that they add positively to each other for maximizing the term $-\sum L_i$ and hence the denominator Δ. For clarity, the idea is illustrated by the addition of one feedback loop from $\tilde{v}_o$ to $\tilde{v}_{co}$, as shown in Fig. 7.

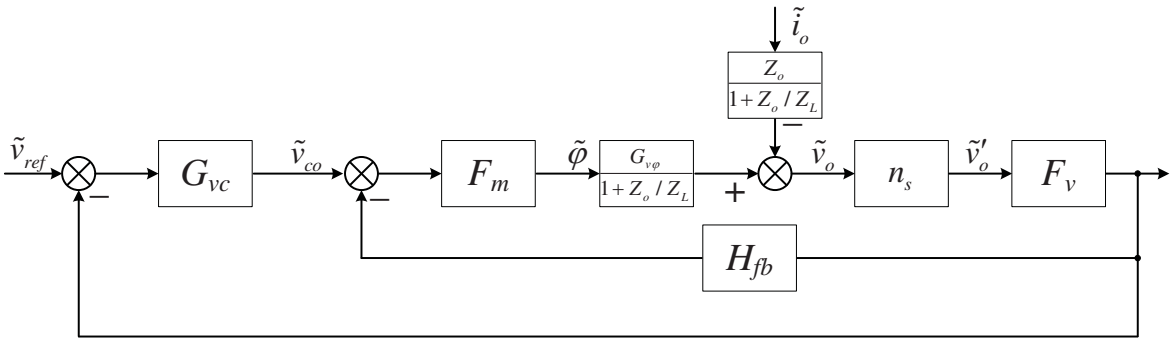

Figure 7: Additional loop created by output-voltage feedback.

By applying the Mason's gain formula, the output voltage $\tilde{v}_o$ produced by the closed-loop system is given by Equation (15), where L is the original loop gain and L_{fb} is the additional loop gain.

$$\begin{aligned} \tilde{v}_o &= \frac{G_{vc}F_m\frac{G_{v\varphi}}{1+Z_o/Z_L}}{1+L+L_{fb}}\tilde{v}_{ref} - \frac{\frac{Z_o}{1+Z_o/Z_L}}{1+L+L_{fb}}\tilde{i}_o \\ L &= G_{vc}F_mF_vn_s\frac{G_{v\varphi}}{1+Z_o/Z_L} \\ L_{fb} &= H_{fb}F_mF_vn_s\frac{G_{v\varphi}}{1+Z_o/Z_L} \end{aligned} \tag{15}$$

By comparing Equation (15) to Equation (12), it can be easily seen that the converter's closed-loop output impedance $\tilde{v}_o/-\tilde{i}_o$ has been reduced due to the additional loop. The amount of reduction depends on the value of the additional loop gain L_{fb}, and different selections of the feedback gain H_{fb} give rise to different closed-loop output-impedance characteristics, as will be discussed later. However, on the other hand, it can be seen from Equation (15) that the additional loop not only decreases the closed-loop output impedance but also affects the converter's closed-loop dynamic response $\tilde{v}_o/\tilde{v}_{ref}$ compared to the original system (Fig. 4). The

This article has been accepted for publication in a future issue of this journal, but has not been fully edited. Content may change prior to final publication. Citation information: DOI 10.1109/TPEL.2014.2369573, IEEE Transactions on Power Electronics

actual effects depend on the specific form of H_{fb} selected for implementing the additional loop.

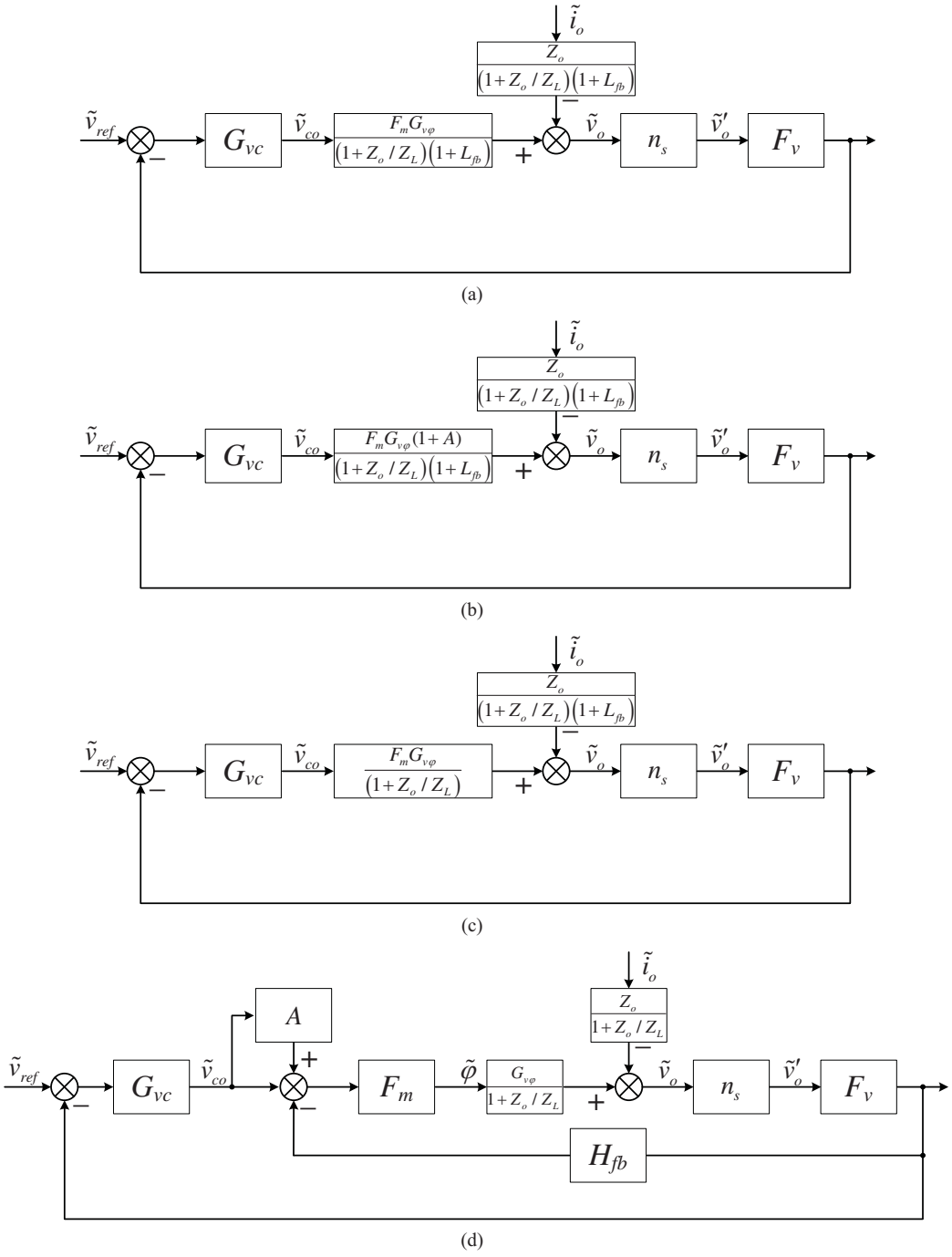

Figure 8: Derivation of method for compensating the effect of additional loop L_{fb} on converter's dynamic response.

In order to reduce the sensitivity of the converter's dynamic response to the additional loop, it is necessary to introduce some compensation into the control system. The nature and form of the compensation can be

This article has been accepted for publication in a future issue of this journal, but has not been fully edited. Content may change prior to final publication. Citation information: DOI 10.1109/TPEL.2014.2369573, IEEE Transactions on Power Electronics

obtained by analyzing the control system of the converter. The first step involves converting the control system shown in Fig. 7 to the equivalent system shown in Fig. 8a. In comparison to Fig. 4, it can be seen that the forward-path gain from $\tilde{v}_{co}$ to $\tilde{v}_o$ is reduced by a factor of $(1 + L_{fb})$. In order to compensate for this effect, an additional forward-path gain of $(1 + A)$ should be introduced into the same path. It is clear that when the condition $A = L_{fb}$ is satisfied, the original forward-path gain from $\tilde{v}_{co}$ to $\tilde{v}_o$ as shown in Fig. 4 is restored, and the compensated system is as shown in Fig. 8c. In practice, the additional forward-path gain of $(1 + A)$ can be realized by the modified system shown in Fig. 8d. In other words, the compensated system will have the same loop gain ($= L$), and hence the same dynamic response, as the original system, while its closed-loop output impedance is reduced by a factor of $(1 + L_{fb})$. For the compensated system, the output voltage $\tilde{v}_o$ produced by the closed-loop system is given by Equation (16), where L and L_{fb} are defined in Equation (15).

$$\tilde{v}_o = \frac{G_{vc}F_m\frac{G_{v\varphi}}{1+Z_o/Z_L}}{1+L}\tilde{v}_{ref} - \frac{\frac{Z_o}{(1+Z_o/Z_L)(1+L_{fb})}}{1+L}\tilde{i}_o \tag{16}$$

Therefore, for the compensated system with additional loop L_{fb}, its closed-loop output impedance is given by Equation (17). By substituting the definition of loop gain L_{fb} given by Equation (15) into Equation (17), remembering that $G_{v\varphi} = G_{i\varphi}Z_o$, Equation (18) is obtained.

$$\begin{aligned} \frac{\tilde{v}_o}{-\tilde{i}_o} &= \frac{\frac{Z_o}{(1+Z_o/Z_L)(1+L_{fb})}}{1+L} \\ &= \frac{\frac{1}{\frac{1}{Z_o}+\frac{1}{Z_L}+L_{fb}\left(\frac{1+Z_o/Z_L}{Z_o}\right)}}{1+L} \end{aligned} \tag{17}$$

$$\frac{\tilde{v}_o}{-\tilde{i}_o} = \frac{\frac{1}{\frac{1}{Z_o}+\frac{1}{Z_L}+H_{fb}F_mF_vn_sG_{i\varphi}}}{1+L} = \frac{\frac{1}{\frac{1}{Z_o}+\frac{1}{Z_L}+\frac{1}{Z_V}}}{1+L} \tag{18}$$

Equation (18) is of significant interest as it implies that the introduction of the additional loop L_{fb} is equivalent to adding impedance in parallel to the existing converter's output impedance (Z_o and Z_L), and thus diminishing the overall converter's output impedance compared to the original system. We name this the "virtual-impedance technique" for output-impedance reduction, with the virtual impedance's value Z_V given by Equation (19). In this equation, the control-to-output-current transfer function $G_{i\varphi}$ is given by Equation (6) and can be approximated as being constant for a nominal φ. The product $F_mF_vn_s$ is also constant for a given converter's design. Thus, the characteristic of Z_V depends only on the specific form of the feedback gain H_{fb} selected, and the choice of H_{fb} conveniently provides a tool for shaping the converter's closed-loop output

This article has been accepted for publication in a future issue of this journal, but has not been fully edited. Content may change prior to final publication. Citation information: DOI 10.1109/TPEL.2014.2369573, IEEE Transactions on Power Electronics

impedance in a deterministic way. In the following parts, the three basic modes of H_{fb}, corresponding to the three fundamental circuit elements, *i.e.* resistor, capacitor, and inductor, will be discussed.

$$Z_V = \frac{1}{H_{fb}F_mF_vn_sG_{i\varphi}} \tag{19}$$

3.3.1 Virtual Resistor

If the feedback gain H_{fb} is chosen to be a pure number X, the resulting Z_V will resemble a resistor of the value given by Equation (20). In other words, a resistor R_V is virtually added in parallel to Z_o and Z_L.

$$Z_{VR} = \frac{1}{XF_mF_vn_sG_{i\varphi}} = R_V \tag{20}$$

In the foregoing discussion, an additional forward-path gain $(1 + A)$ must be placed between the G_{vc}-block and the adjacent summing node for restoring the converter's dynamic response after the additional loop L_{fb} is added, where

$$A = L_{fb} = \frac{XF_mF_vn_sG_{v\varphi}}{1 + Z_o/Z_L} \tag{21}$$

Typically, the condition $Z_o \ll Z_L$, or $Z_o/Z_L \ll 1$, holds, hence the implementation of the additional forward-path gain is considerably simplified by making it load-independent, *i.e.* $A \approx XF_mF_vn_sG_{v\varphi}$. The compensated system with $H_{fb} = X$ is shown in Fig. 9, and the Bode plots of the overall converter's loop gain with/without virtual-resistor implementation and with/without forward-path-gain compensation are shown in Fig. 10. The corresponding plots of open-loop and closed-loop output-impedance are shown in Fig. 11. It is evident from the gain plots in Fig. 10 that without introducing the additional forward-path gain $(1 + A)$ the low-frequency loop gain is significantly attenuated, which will have negative effects on the converter's dynamic response.

It can be seen from Fig. 11 that, in general, the closed-loop output impedance decreases as the virtual resistance decreases. However, this mainly affects the low-frequency region only. In proximity to the frequency of interest (100 Hz), the output impedance is dominated by Z_o and Z_L, and is essentially unaffected by the value of the virtual resistor. This renders the virtual-resistor approach ineffective in reducing the converter's output impedance as seen by the 100-Hz voltage ripple on the dc bus voltage.

This article has been accepted for publication in a future issue of this journal, but has not been fully edited. Content may change prior to final publication. Citation information: DOI 10.1109/TPEL.2014.2369573, IEEE Transactions on Power Electronics

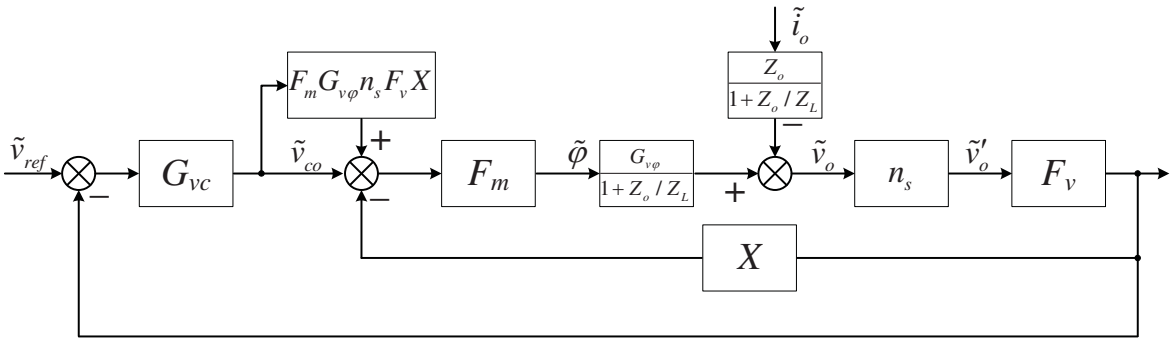

Figure 9: Control system of the converter used in the energy storage branch implemented with virtual resistor.

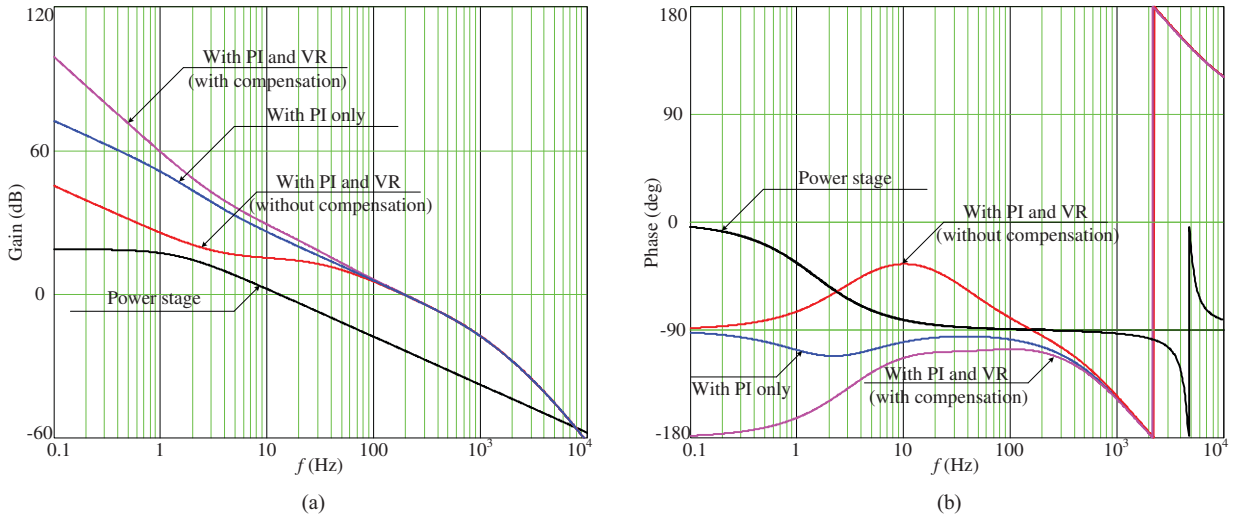

Figure 10: Bode plots of converter's loop gain with/without virtual-resistor implementation and with/without forward-path-gain compensation.

3.3.2 Virtual Capacitor

Another option is to choose the feedback gain H_{fb} to be a pure derivative term in the form of sX, the resulting Z_V will resemble a capacitor of the value given by Equation (22). In other words, a capacitor C_V is virtually added in parallel to Z_o and Z_L.

$$\begin{aligned} Z_{VC} &= \frac{1}{sXF_mF_vn_sG_{i\varphi}} = \frac{1}{sC_V} \\ C_V &= XF_mF_vn_sG_{i\varphi} \end{aligned} \tag{22}$$

Similar to the virtual-resistor case, an additional forward-path gain $(1 + A)$ must be placed between the

This article has been accepted for publication in a future issue of this journal, but has not been fully edited. Content may change prior to final publication. Citation information: DOI 10.1109/TPEL.2014.2369573, IEEE Transactions on Power Electronics

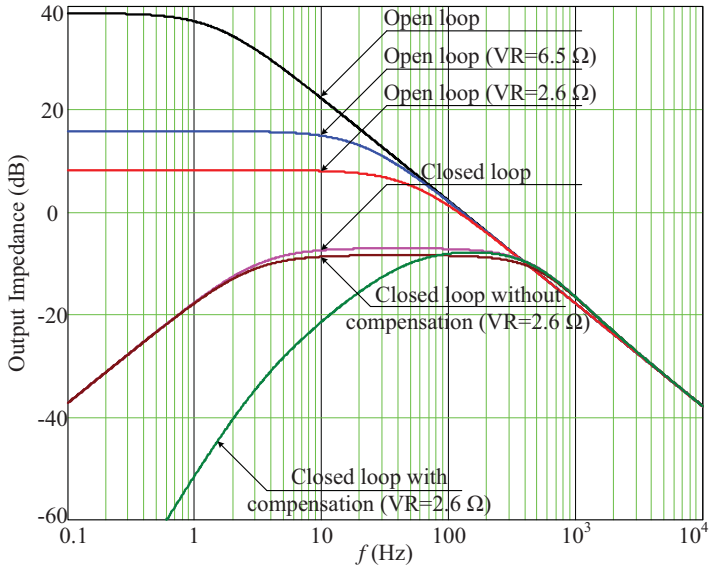

Figure 11: Plots of converter's open-loop and closed-loop output impedance with/without virtual-resistor implementation and with/without forward-path-gain compensation.

G_{vc}-block and the adjacent summing node, with X replaced by sX and the same assumption of $Z_o/Z_L \ll 1$ is made.

$$A = L_{fb} = \frac{sXF_mF_vn_sG_{v\varphi}}{1 + Z_o/Z_L} \approx sXF_mF_vn_sG_{v\varphi} \tag{23}$$

The compensated system with $H_{fb} = sX$ is shown in Fig. 12, and the Bode plots of the overall converter's loop gain with/without virtual-resistor implementation and with/without forward-path-gain compensation are shown in Fig. 13. The corresponding plots of open-loop and closed-loop output-impedance are shown in Fig. 14.

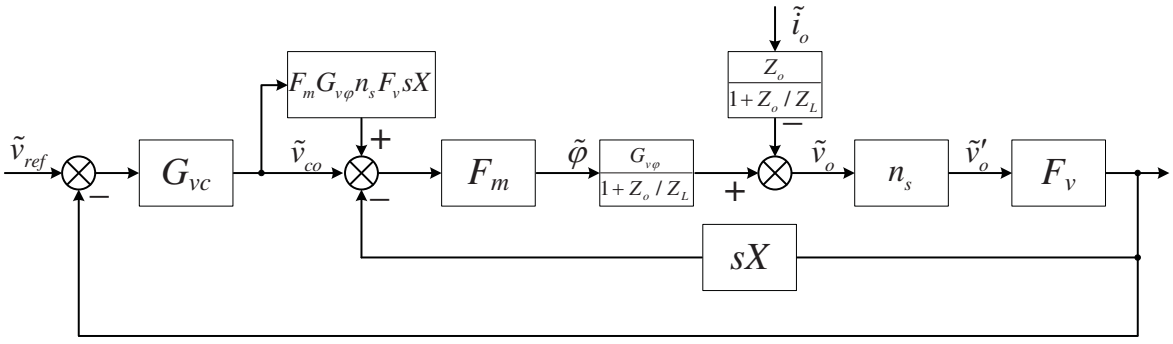

Figure 12: Control system of the converter used in the energy storage branch implemented with virtual capacitor.

It can be seen that without introducing the additional forward-path gain $(1 + A)$ the loop gain's crossover frequency is reduced from 200 Hz (for the original system) to about 50 Hz; it is restored to the original value after

This article has been accepted for publication in a future issue of this journal, but has not been fully edited. Content may change prior to final publication. Citation information: DOI 10.1109/TPEL.2014.2369573, IEEE Transactions on Power Electronics

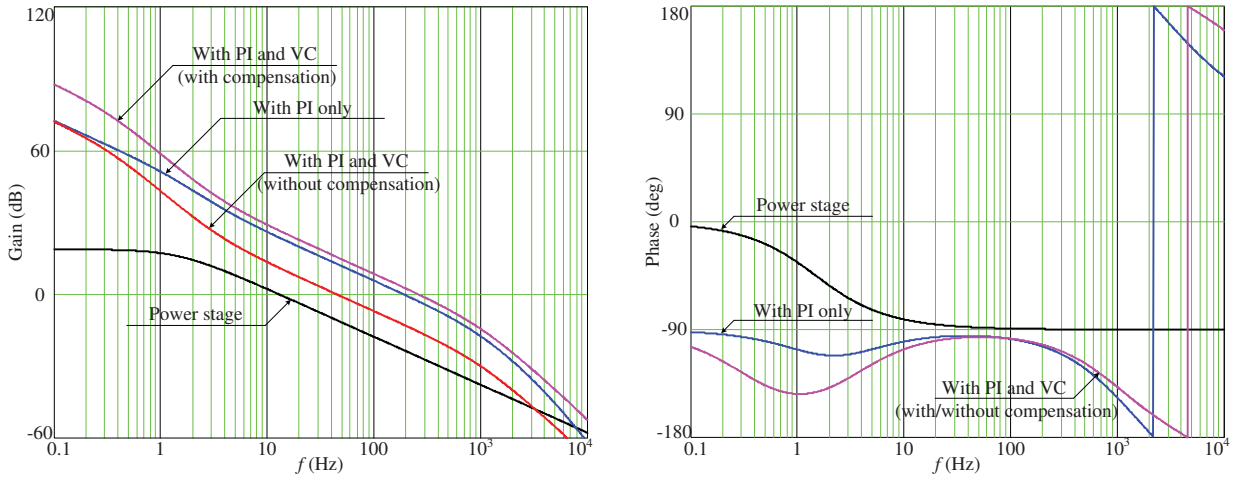

Figure 13: Bode plots of converter's loop gain with/without virtual-capacitor implementation and with/without forward-path-gain compensation.

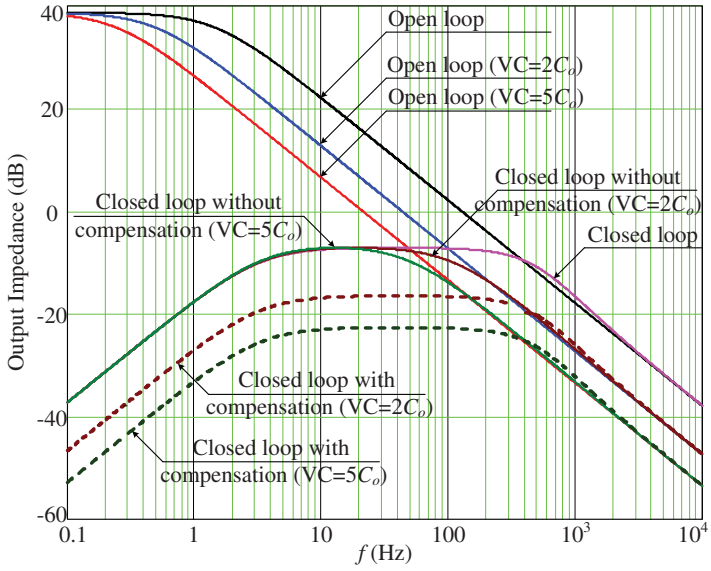

Figure 14: Plots of converter's open-loop and closed-loop output impedance with/without virtual-capacitor implementation and with/without forward-path-gain compensation.

the additional forward-path gain is introduced so that the converter's dynamic response is not unintentionally sacrificed due to the additional loop L_{fb}. From Fig. 14, it is evident that the additional forward-path gain $(1+A)$ not only restores the converter's dynamic response but also enhances the effect of the additional loop L_{fb} and further attenuates the closed-loop output impedance of the converter (see dashed lines). In general, the degree of attenuation increases as the virtual capacitance increases.

This article has been accepted for publication in a future issue of this journal, but has not been fully edited. Content may change prior to final publication. Citation information: DOI 10.1109/TPEL.2014.2369573, IEEE Transactions on Power Electronics

3.3.3 Virtual Inductor

Finally, if the feedback gain H_{fb} is chosen to be a pure integration term of the form X/s, the resulting Z_V will resemble an inductor of the value given by Equation (24). In other words, an inductor L_V is virtually added in parallel to Z_o and Z_L.

$$\begin{aligned} Z_{VL} &= \frac{s}{XF_mF_vn_sG_{i\varphi}} = sL_V \\ L_V &= \frac{1}{XF_mF_vn_sG_{i\varphi}} \end{aligned} \tag{24}$$

Similar to the previous two cases, an additional forward-path gain $(1 + A)$ must be placed between the G_{vc}-block and the adjacent summing node, with X replaced by X/s and the same assumption of $Z_o/Z_L \ll 1$ is made.

$$A = L_{fb} = \frac{XF_mF_vn_sG_{v\varphi}}{s\,(1 + Z_o/Z_L)} \approx \frac{XF_mF_vn_sG_{v\varphi}}{s} \tag{25}$$

The compensated system with $H_{fb} = X/s$ is shown in Fig. 15, and the Bode plots of the overall converter's loop gain with/without virtual-resistor implementation and with/without forward-path-gain compensation are shown in Fig. 16. The corresponding plots of open-loop and closed-loop output-impedance are shown in Fig. 17.

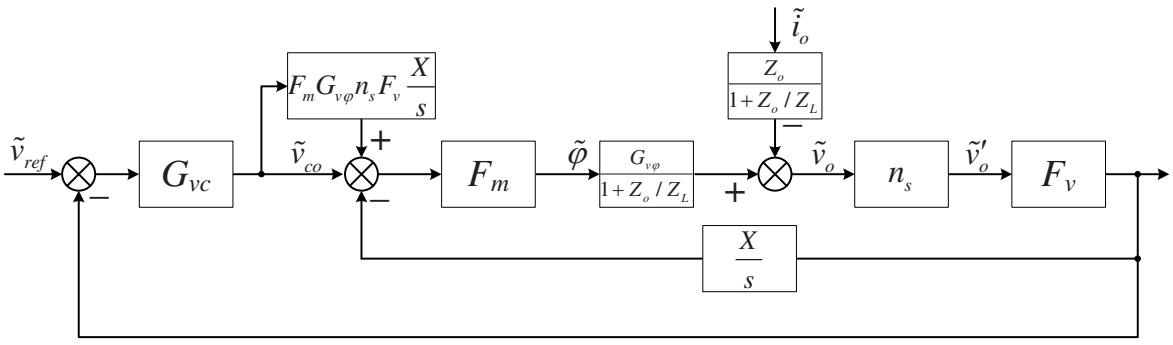

Figure 15: Control system of the converter used in the energy storage branch implemented with virtual inductor.

It can be seen that while the loop gain's crossover frequency remains essentially unaffected, the loop gain's behavior below the crossover frequency has been completely altered by the presence of the virtual inductor. The addition of forward-path gain $(1 + A)$ restores the loop gain to one close to the original system. As expected, with the addition of virtual inductor in parallel with Z_o and Z_L, both open-loop and closed-loop output-impedance characteristics exhibit resonance peaks due to the resonance between the output capacitor C_o

This article has been accepted for publication in a future issue of this journal, but has not been fully edited. Content may change prior to final publication. Citation information: DOI 10.1109/TPEL.2014.2369573, IEEE Transactions on Power Electronics

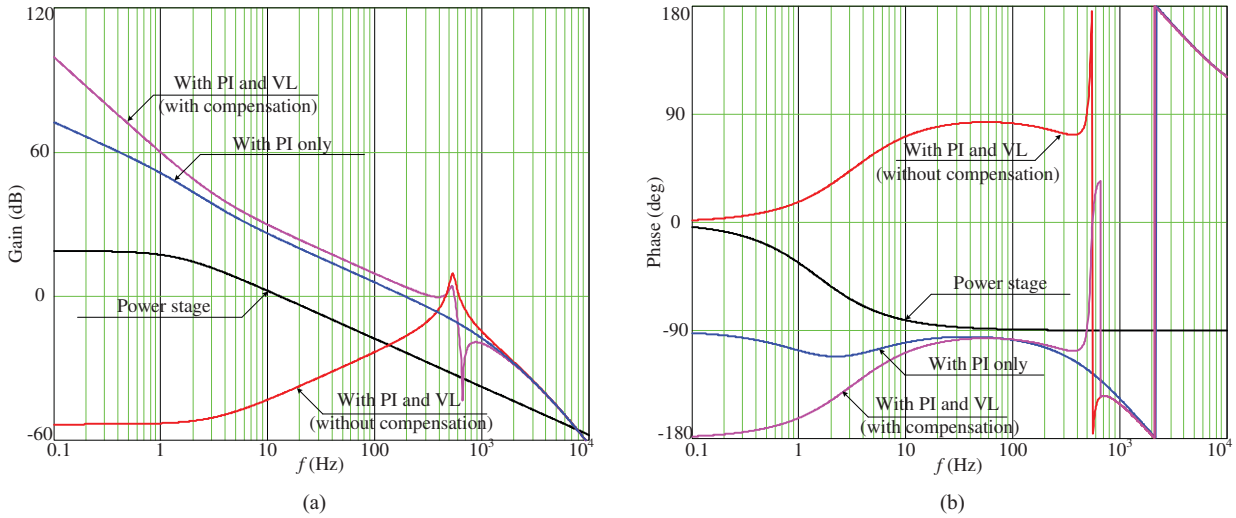

Figure 16: Bode plots of converter's loop gain with/without virtual-inductor implementation and with/without forward-path-gain compensation.

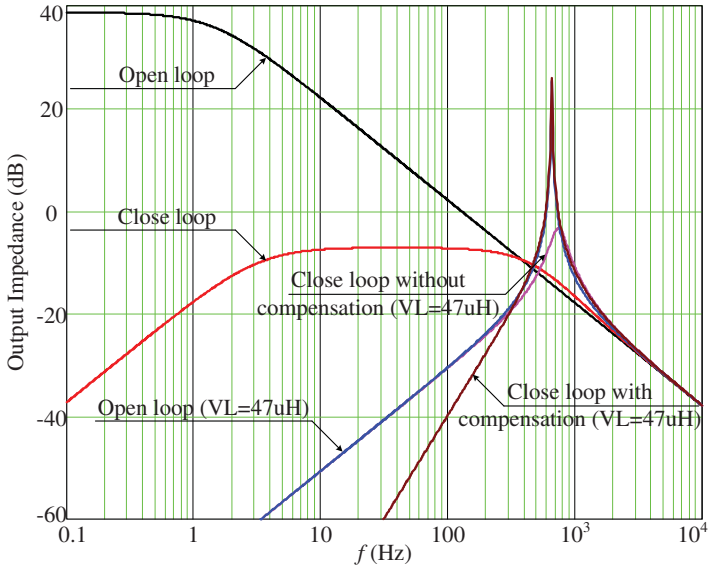

Figure 17: Plots of converter's open-loop and closed-loop output impedance with/without virtual-inductor implementation and with/without forward-path-gain compensation.

and the virtual inductor L_V. Below the resonant frequency, the converter's output impedance is inductive which favors a strongly attenuated low-frequency output-impedance characteristic.

In summary, load-current feed-forward and output-voltage feedback constitute two possible routes to converter's output-impedance reduction, according to the Mason's gain formula, where the former decreases the numerator while the latter increases the denominator. The output-voltage feedback method involves forming

This article has been accepted for publication in a future issue of this journal, but has not been fully edited. Content may change prior to final publication. Citation information: DOI 10.1109/TPEL.2014.2369573, IEEE Transactions on Power Electronics

an additional loop and gives rise to three basic modes of implementation, all of which resemble the paralleling of an additional impedance (*i.e.* virtual impedance) to the existing physical converter's output impedance. All of them are capable of reducing the converter's closed-loop output impedance but with different degrees of effectiveness. From the converter's Bode plots, it is evident that the introduction of additional forward-path gain is mandatory for compensating the negative effects that arise naturally from the actions of the additional loop (L_{fb}) on the converter's dynamic response.

4 Design and Practical Implementation

In this section, the circuit design and practical implementation of the four basic modes of output-impedance shaping method derived in the last section are presented. For the two-input bidirectional DAB dc-dc converter discussed in Section 2, its practical controller's design based on phase-shift PWM control is shown in Fig. 18.

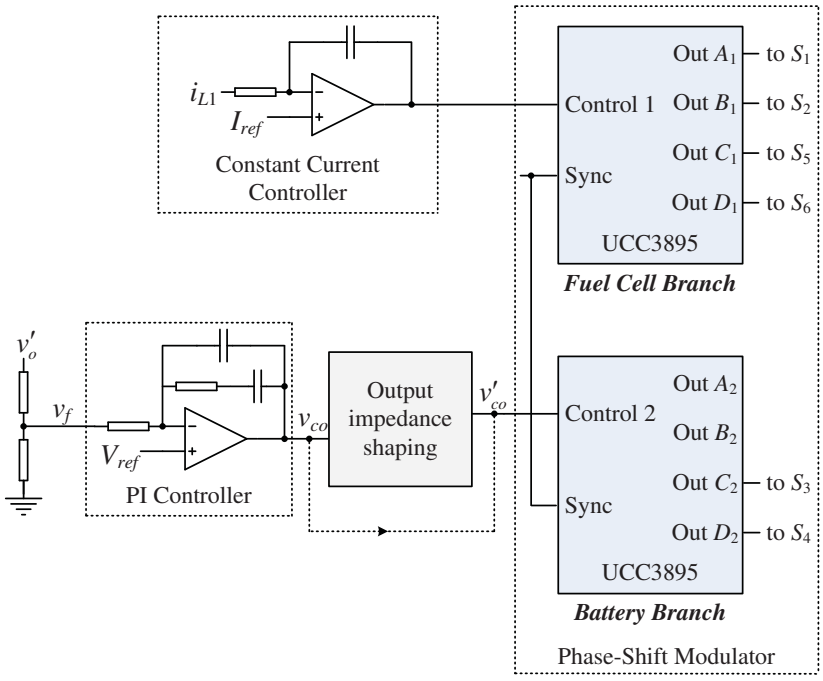

Figure 18: Practical controller's design for a two-input bidirectional DAB dc-dc converter system.

Since six gate driving signals are required to operate the converter, two UCC3895 phase-shift PWM controllers are used and synchronized by referencing to the transformer's secondary-side voltage. The fuel cell branch is controlled by a simple PI-based constant-current regulator which generates the gate driving signals for the primary-side half-bridge's MOSFETs (S_1 and S_2 of the fuel cell branch) and the shared secondary-side half-bridge's MOSFETs (S_5 and S_6). The energy storage (battery) branch is in turn controlled by a PI-based

This article has been accepted for publication in a future issue of this journal, but has not been fully edited. Content may change prior to final publication. Citation information: DOI 10.1109/TPEL.2014.2369573, IEEE Transactions on Power Electronics

voltage regulator cascaded with the output-impedance shaping circuit which generates the gate driving signals for the primary-side half-bridge's MOSFETs (S_3 and S_4 of the battery branch). According to the foregoing discussions, the additional forward path (for load-current feed-forward) or feedback loop (for output-voltage feedback) is added to the control signal v_{co}. As the additional forward-path gain $(1 + A)$ also acts on the same control signal v_{co}, it can be easily included as part of the output-impedance shaping circuit in the present implementation. The control signal emerging from the output-impedance shaping circuit is the modified control signal v'_{co}. The output-impedance shaping circuit can also be bypassed by short-circuiting v_{co} and v'_{co}.

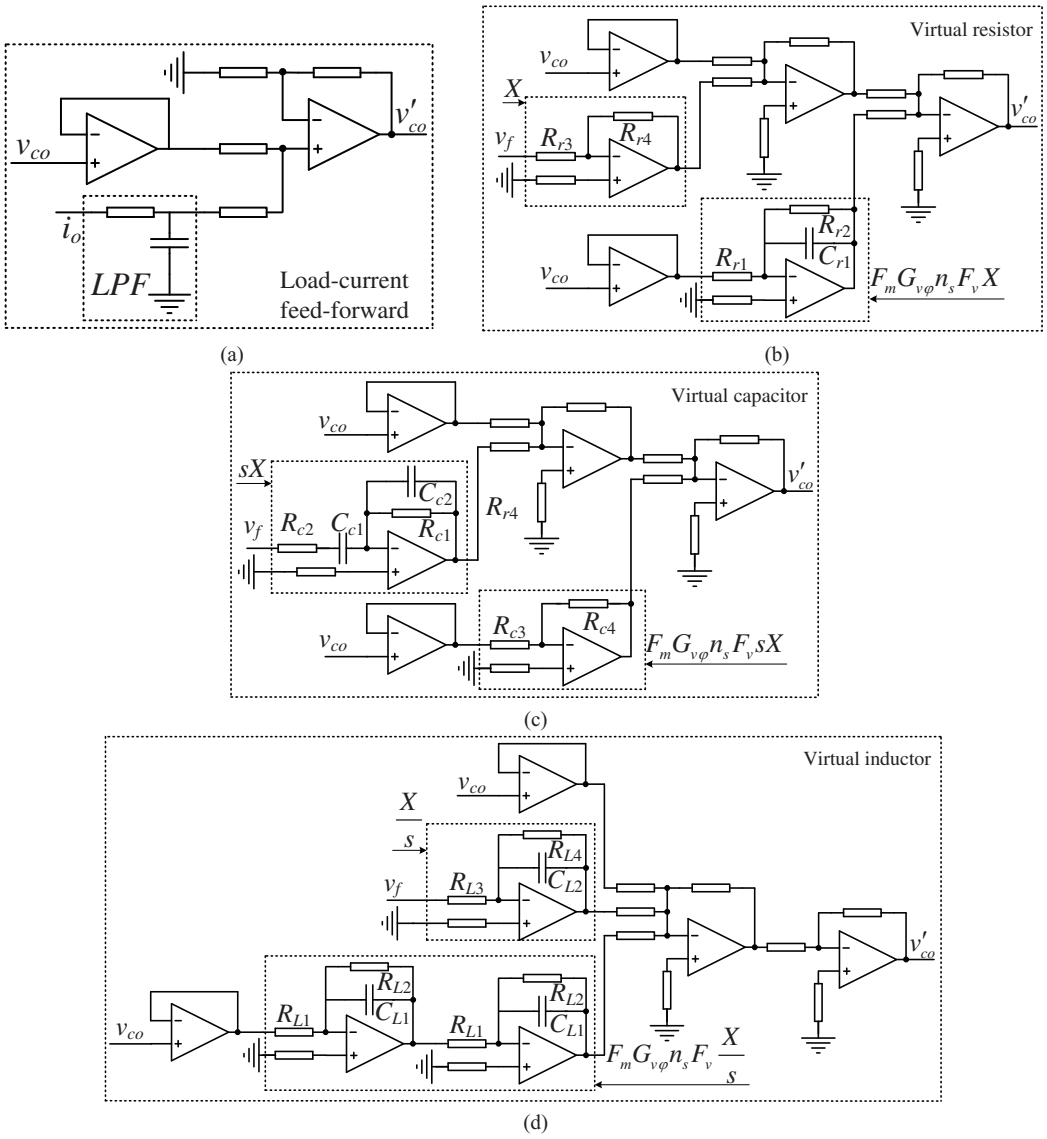

Figure 19: Practical implementation of output-impedance shaping circuit for: (a) load-current feed-forward; (b) virtual resistor; (c) virtual capacitor; and (d) virtual inductor.

This article has been accepted for publication in a future issue of this journal, but has not been fully edited. Content may change prior to final publication. Citation information: DOI 10.1109/TPEL.2014.2369573, IEEE Transactions on Power Electronics

The load-current feed-forward approach can be implemented with a very simple circuit configuration, as it does not affect the converter's dynamic response and, therefore, there is no need to introduce the additional forward-path gain A. Its practical implementation is shown in Fig. 19a, where a non-inverting summing amplifier is used to add the sampled load current to the control signal. The load current is sampled using a Hall sensor cascaded with a low-pass filter for removing high-frequency noises.

Fig. 19b shows the practical implementation of the virtual-resistor-based approach. The feedback gain $H_{fb} = X$ is implemented using a simple inverting amplifier with a gain of $R_{r4}/R_{r3} = X$. In practice, in order to avoid saturation of the inverting amplifier's output, the value of X, or in other words the amplifier's gain R_{r4}/R_{r3}, should be restricted by the amplifier's supply voltage. From Equation (26), it can be seen that the required additional forward-path gain A can be implemented using an integrator with its components R_{r1} and C_{r1} determined from the simple relation $R_{r1}C_{r1} = R_V C_o$. The feedback resistor R_{r2} is included to avoid saturation of the integrator's output.

$$A \approx XF_mF_vn_sG_{v\varphi} = \frac{XF_mF_vn_sG_{i\varphi}}{sC_o} = \frac{1}{sR_VC_o} = \frac{1}{sR_{r1}C_{r1}} \tag{26}$$

Fig. 19c shows the practical implementation of the virtual-capacitor-based approach. In this case, the feedback gain $H_{fb} = sX$ is implemented using a differentiator with a theoretical gain of $sR_{c1}C_{c1} = sX$. Although the values of R_{c1} and C_{c1} should be determined from this theoretical gain, a more practical version of the differentiator requires the inclusion of R_{c2} and C_{c2} for attenuating high-frequency noises. From Equations (22) and (23), the additional forward-path gain A can be rewritten as C_V/C_o, which shows that it can be implemented using a simple inverting amplifier with a gain of $C_V/C_o = R_{c4}/R_{c3}$. It can also be seen from Equation (27) that the virtual capacitance increases proportionally with the feedback gain $|H_{fb}|$.

$$A \approx sXF_mF_vn_sG_{v\varphi} = \frac{XF_mF_vn_sG_{i\varphi}}{C_o} = \frac{C_V}{C_o} = \frac{R_{c4}}{R_{c3}} \tag{27}$$

Finally, the virtual-inductor-based approach is implemented using the circuit shown in Fig. 19d. The feedback gain $H_{fb} = X/s$ is implemented using an integrator with a theoretical gain of $1/sR_{L3}C_{L2} = X/s$. The feedback resistor R_{L4} is included to avoid saturation of the integrator's output. From Equations (24) and (25), the additional forward-path gain A can be rewritten as $1/s^2L_VC_o$, and this enables its implementation using two cascaded integrators of equal gains, as shown in Fig. 19d, where $R_{L1}C_{L1} = \sqrt{L_VC_o}$. Again, the feedback resistor R_{L2} is included to avoid saturation of the integrators' outputs.

This article has been accepted for publication in a future issue of this journal, but has not been fully edited. Content may change prior to final publication. Citation information: DOI 10.1109/TPEL.2014.2369573, IEEE Transactions on Power Electronics

$$A \approx \frac{XF_mF_vn_sG_{v\varphi}}{s} = \frac{XF_mF_vn_sG_{i\varphi}}{s^2C_o} = \frac{1}{s^2L_VC_o} = \frac{1}{s^2\left(R_{L1}C_{L1}\right)^2} \tag{28}$$

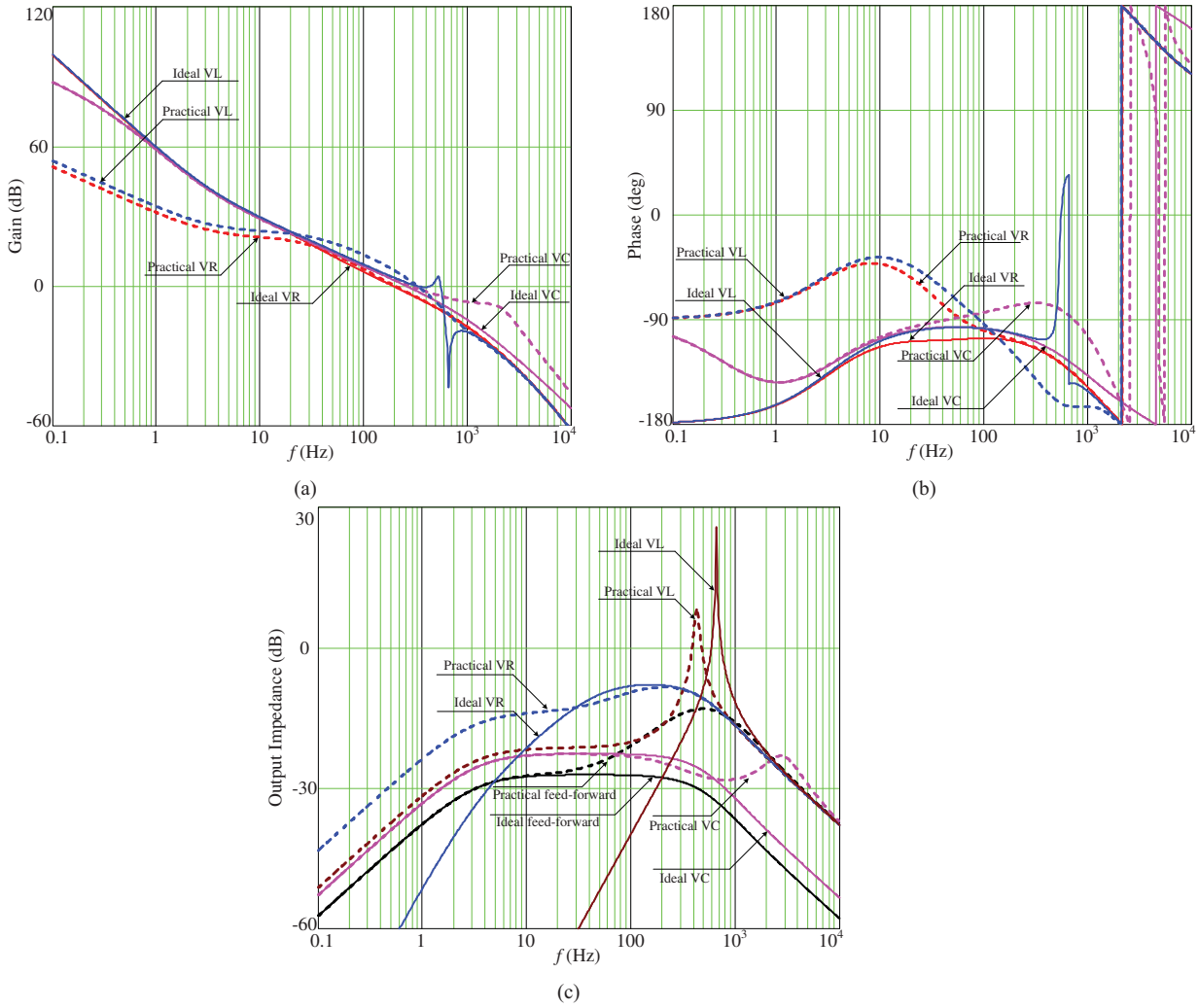

Figure 20: Bode plots of converter's loop gain and output impedance with ideal and practical implementations of various output-impedance shaping methods: (a) magnitude; (b) phase; and (c) closed-loop output impedance.

Fig.20 shows the Bode plots of the converter's loop gain and closed-loop output impedance with ideal and practical implementation of the various output-impedance shaping methods. The main difference between the theoretical and practical case is caused by the use of non-ideal integrator or differentiator in the implementation. For the case of load-current feed-forward, the deviation from the ideal case at high frequencies is due to the use of low-pass filter in sampling the load current (see Fig. 19a). At high frequencies, the sampled load current becomes severely attenuated by the low-pass filter and the feed-forward path is rendered effectively open circuit.

This article has been accepted for publication in a future issue of this journal, but has not been fully edited. Content may change prior to final publication. Citation information: DOI 10.1109/TPEL.2014.2369573, IEEE Transactions on Power Electronics

5 Experimental Results

In this section, the performances of the various modes of output-impedance shaping are evaluated. For this purpose, a prototype of two-input bidirectional DAB dc-dc converter with output-impedance shaping capability is constructed with the specifications listed in Table 1. In the experimental system, the fuel cell unit is emulated using a dc power supply that delivers a constant current, hence constant power, to the system. To avoid low-frequency harmonic current being drawn from the fuel cell branch, its closed-loop bandwidth is designed to be 7 Hz, *i.e.* $<$ 1/10 of the harmonic frequency at 100 or 120 Hz. For the energy storage branch, a battery bank made of lead-acid batteries is used, with four 12-V, 18-Ah batteries connected in series. The closed-loop bandwidth of the battery branch is designed to be approximately 190 Hz, which is well below the frequency (4.8 kHz) of the RHP zeros and poles on the imaginary axis. The inverter is a conventional one based on full-bridge topology driven by sinusoidal PWM. Note that a small output dc-link capacitor (20 μF) is intentionally used to generate significant voltage ripple on the dc bus voltage so that its reduction by output-impedance shaping can be more clearly visualized afterwards.

Table 1: Specifications of the two-input bidirectional DAB dc-dc converter prototype.

Description	*Parameter*	*Value*
Fuel cell's output power	P_{fc}	160 W
Fuel cell's terminal voltage	V_{fc}	20 V
Transformer's leakage inductance (fuel cell branch)	L_{r1}	4.7 μH
Transformer's turn ratio (fuel cell branch)	$N_{p1} : N_{s1}$	1:10
Dc-link capacitor for input half-bridge (fuel cell branch)	C_{p1}	80 μF
Maximum battery power	P_{bat}	160 W
Battery's terminal voltage	V_{bat}	48 V
Transformer's leakage inductance (battery branch)	L_{r2}	25.5 μH
Transformer's turn ratio (battery branch)	$N_{p2} : N_{s2}$	6:25
Dc-link capacitor for input half-bridge (battery branch)	C_{p2}	5 μF
Dc-link capacitor for secondary half-bridge	C_s	100 μF
Output dc bus voltage	V_o	400 V
Output dc-link capacitor	C_o	20 μF
Switching frequency	f_{sw}	52 kHz

Before discussing the experimental results, the selection of parameters for implementing the various modes of output-impedance shaping methods are explained. It should be emphasized that these parameters are not optimized in any way, and, as it will be shown, they are determined solely for the mode under consideration. Although there clearly exists the possibility of combining various modes in one particular implementation, no effort is made here to study all possible combinations and to search for the optimum solution or to propose

This article has been accepted for publication in a future issue of this journal, but has not been fully edited. Content may change prior to final publication. Citation information: DOI 10.1109/TPEL.2014.2369573, IEEE Transactions on Power Electronics

a generalized design approach (such a solution or design approach may or may not exist), as this paper aims only to communicate the four basic modes of output-impedance shaping method that have already been shown to emerge naturally from the Mason's gain formula. In addition, it should be clear that these methods are not applicable to the type of converter discussed in this paper only, and that they can be adopted in different ways by systems requiring output-impedance shaping for fulfilling specific practical needs, which are too many and cannot be fully explored here.

For the load-current feed-forward approach, the ideal choice is $H_{fd} = H_{fd0}$, but to account for the component tolerances, $H_{fd} = 0.9H_{fd0}$ is chosen to ensure that the output impedance remains always positive. For the virtual-resistor approach, it was discussed previously that the choice of feedback gain $H_{fb} = X$ is limited by the supply voltage (V_{cc}) of the inverting amplifier used for realizing X. With $V_{ref} = 4.5$ V and $V_{cc} = 12$ V, X is limited to the maximum value of 2.67, and $X = 2.5$ is chosen for the experimental system, which gives $R_V = 2.6\ \Omega$. For the virtual-capacitor approach, the virtual capacitance should be chosen such that $C_V \gg C_o$ to ensure that the overall output impedance of the converter is insensitive to its intrinsic output impedance $Z_o = 1/sC_o$. The choice of $C_V = 5C_o$ satisfies this requirement without causing a substantial reduction in v_{co}, thus a good signal-to-noise ratio is preserved. Finally, for the virtual-inductor approach, it is required that the resonance between the converter's output capacitor C_o and the virtual inductor L_V should occur above the desired loop gain's crossover frequency for closed-loop stability, considering that it will introduce an additional 180^{o} phase lag to the loop gain. In general, decreasing the value of L_V shifts the resonant peak to higher frequencies. To achieve a closed-loop bandwidth of about 190 Hz, it is found that the virtual inductance should be set smaller than $47\ \mu$H. The boundary case of $L_V = 47\ \mu$H is chosen for the experimental system.

The steady-state waveforms of the converter implemented with the various modes of output-impedance shaping are shown in Fig. 21a–21e. The case with no output-impedance shaping (*i.e.* using PI controller only) is also included for comparison. For the four waveforms shown in each figure, i_{fc} is the fuel cell's output current, i_{bat} is the battery's output current, $v_{o(dc)}$ is the dc bus voltage, and $v_{o(inv)}$ is the inverter's output voltage. For the dc bus voltage, only the ac-coupled waveform is shown in order to give a magnified and clear view of the voltage ripple component. In all cases, no noticeable harmonic current at the double-line frequency is drawn from the fuel cell branch due to its very small closed-loop bandwidth, hence the harmonic current mainly flows from the dc-link capacitor and the battery branch only. In comparison to the converter using PI controller only, the implementation of the various modes of output-impedance shaping has caused different degrees of reduction in the converter's closed-loop output impedance. This is verified by the reduction in the amplitude of the voltage ripple on the dc bus voltage. The quantitative changes in the voltage ripple's amplitude

This article has been accepted for publication in a future issue of this journal, but has not been fully edited. Content may change prior to final publication. Citation information: DOI 10.1109/TPEL.2014.2369573, IEEE Transactions on Power Electronics

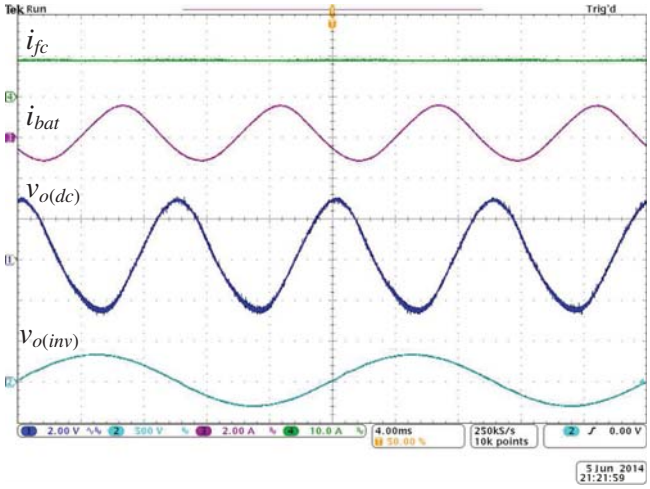

(a)

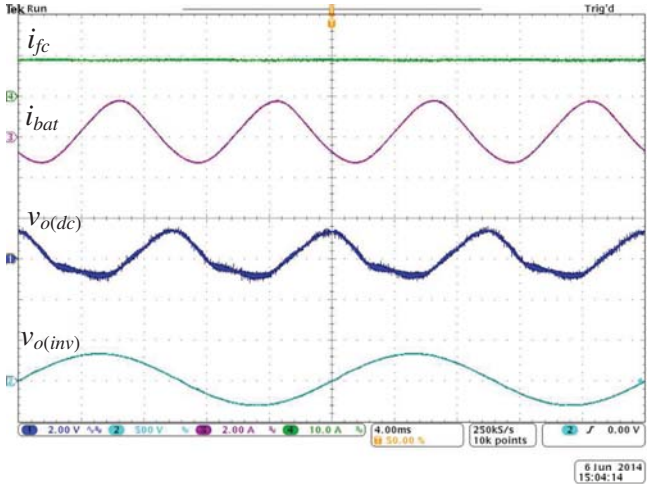

(b)

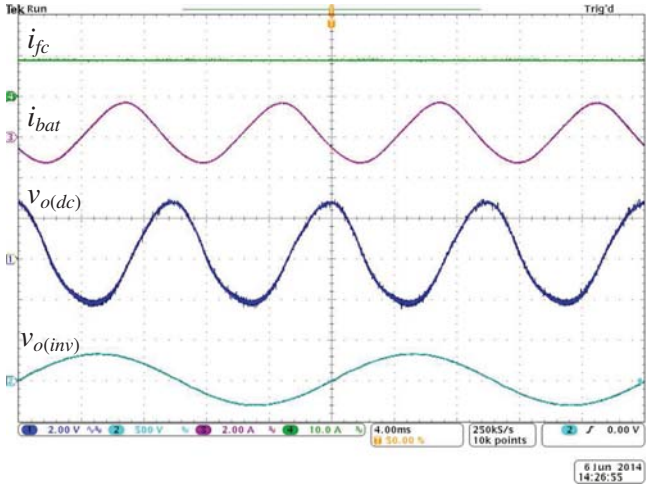

(c)

Figure 21: Static converter waveforms with (a) PI only; (b) PI and load-current feed-forward; and (c) PI and virtual resistor.

This article has been accepted for publication in a future issue of this journal, but has not been fully edited. Content may change prior to final publication. Citation information: DOI 10.1109/TPEL.2014.2369573, IEEE Transactions on Power Electronics

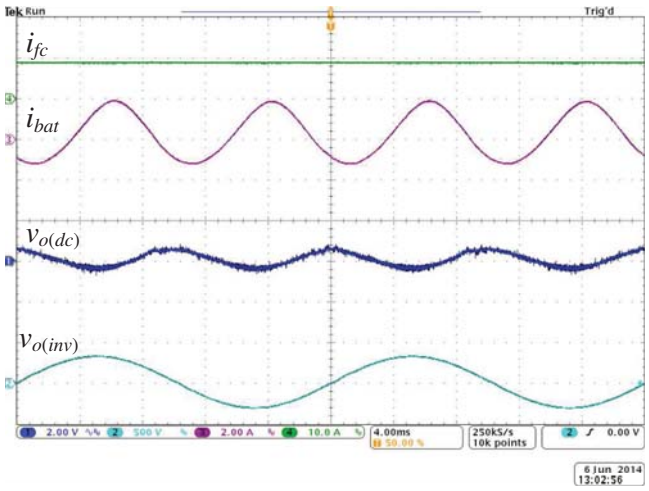

(d)

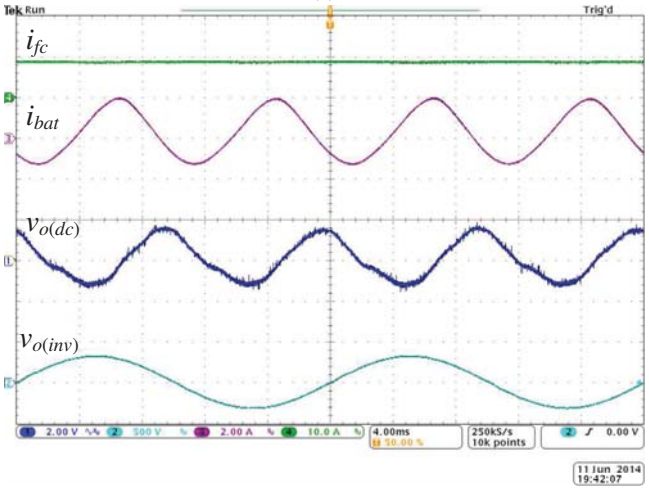

(e)

Figure 21: Static converter waveforms with (d) PI and virtual capacitor; and (e) PI and virtual inductor.

This article has been accepted for publication in a future issue of this journal, but has not been fully edited. Content may change prior to final publication. Citation information: DOI 10.1109/TPEL.2014.2369573, IEEE Transactions on Power Electronics

can be more conveniently visualized from the FFT spectra of the dc bus voltage waveforms, which are shown in Fig. 22a–22e for the various modes of output-impedance shaping. In comparison to the case with PI controller only, the voltage ripple's amplitude has been reduced by 69.5%, 13.9%, 85.0%, and 62.8%, respectively, for the load-current feed-forward, virtual resistor, virtual capacitor, and virtual inductor approach. The measured trend is in agreement with the percentage reduction in output impedance predicted by theoretical analysis, which gives 79.3%, 22.6%, 83.2%, and 77.2% for the corresponding approach. These values are obtained by reading the converter's closed-loop output impedance with PI only (–7.24 dB, from Fig. 6) and with various output impedance shaping methods (–20.9 dB, –9.47 dB, –22.78 dB, and –20.12 dB for load-current feed-forward, virtual resistor, virtual capacitor, and virtual inductor, respectively, from Fig. 20c). The small increase in the battery's output current giving rise to a large reduction in voltage ripple should not be seen as a contradiction, but the result of using a small dc-link capacitor that makes its voltage sensitive to the changes in its stored charge, *i.e.* $\Delta V = \Delta Q/C_o$. The effectiveness of the various modes of output-impedance shaping in reducing voltage ripple's amplitude are in agreement with the closed-loop output impedance associated with them shown in Fig. 20c. At 100 Hz, the virtual-capacitor and virtual-resistor approach results in the smallest and the largest converter's output impedance, respectively, while the load-current feed-forward and virtual-inductor approach perform similarly in this respect.

Finally, the dynamic response of the converter implemented with the various modes of output-impedance shaping were tested and the results are shown in Fig. 23a–23e. In all cases, the inverter's load was stepped from half-load to full-load. It can be seen that before the step-load occurred, the average battery's current was negative, indicating that the battery bank was charged by the fuel cell branch, which delivers a constant power. After the step-load occurred, the average battery's current became approximately zero as the fuel cell branch's output power was balanced by the inverter's load power. It is also clear from these waveforms that the ac component of the battery's output current was nearly doubled in amplitude after the inverter's load was stepped to full-load, while the voltage ripple's amplitude only increased by small increment, which gives a clear indication that the dc-link capacitor's impedance is significantly larger than that of the battery branch at the double-line frequency, as intended by design. In comparison to the converter using PI controller only, the use of various modes of output-impedance shaping did not alter the converter's dynamic response noticeably, in some cases it was even improved, as a result of the simultaneous implementation of the additional forward-path-gain compensation.

This article has been accepted for publication in a future issue of this journal, but has not been fully edited. Content may change prior to final publication. Citation information: DOI 10.1109/TPEL.2014.2369573, IEEE Transactions on Power Electronics

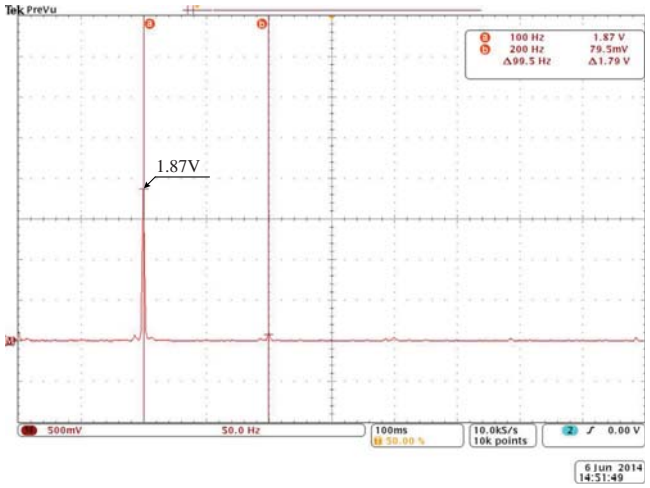

(a)

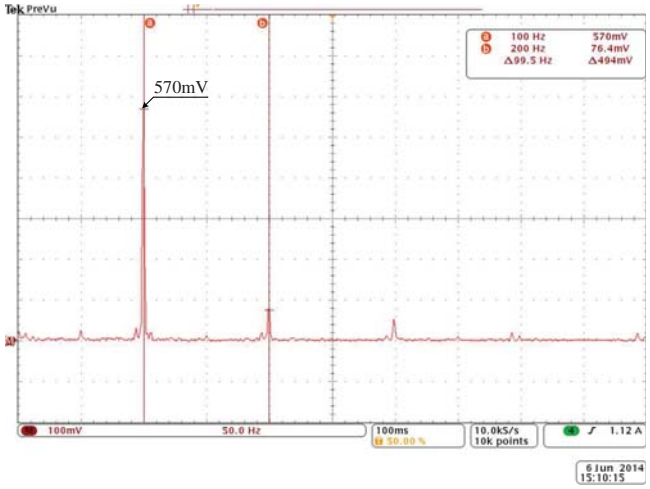

(b)

(c)

Figure 22: FFT analysis of the dc bus voltage with (a) PI only; (b) PI and load-current feed-forward; and (c) PI and virtual resistor.

This article has been accepted for publication in a future issue of this journal, but has not been fully edited. Content may change prior to final publication. Citation information: DOI 10.1109/TPEL.2014.2369573, IEEE Transactions on Power Electronics

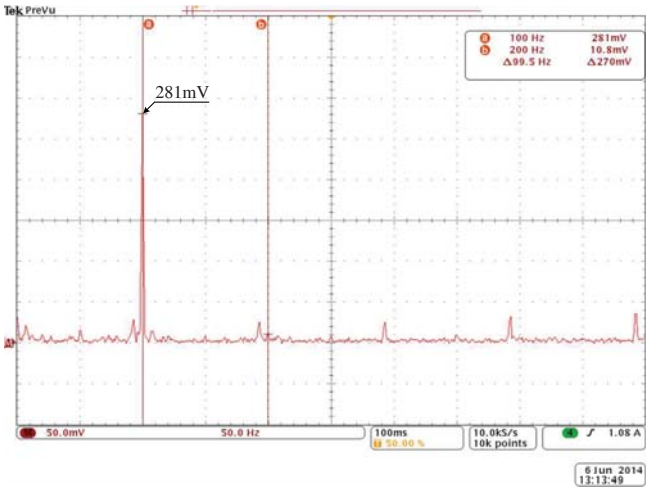

(d)

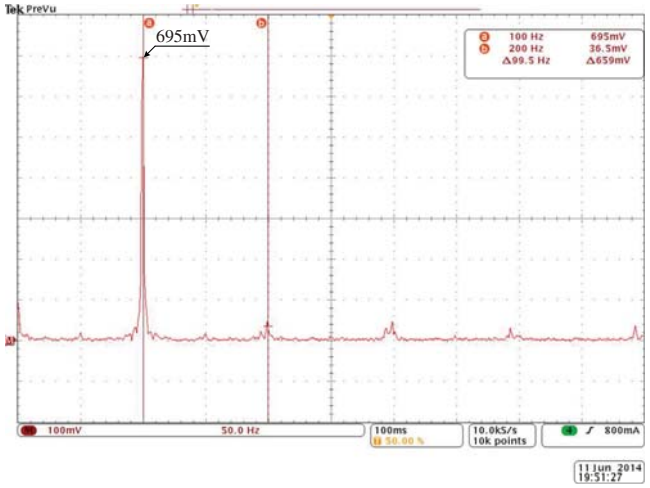

(e)

Figure 22: FFT analysis of the dc bus voltage with (d) PI and virtual capacitor; and (e) PI and virtual inductor.

This article has been accepted for publication in a future issue of this journal, but has not been fully edited. Content may change prior to final publication. Citation information: DOI 10.1109/TPEL.2014.2369573, IEEE Transactions on Power Electronics

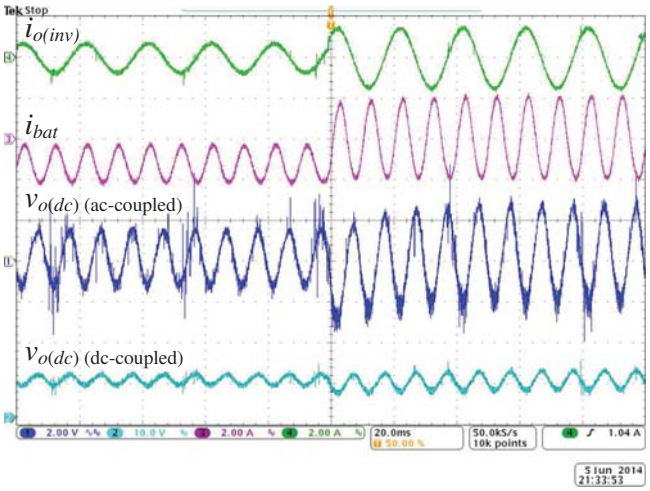

(a)

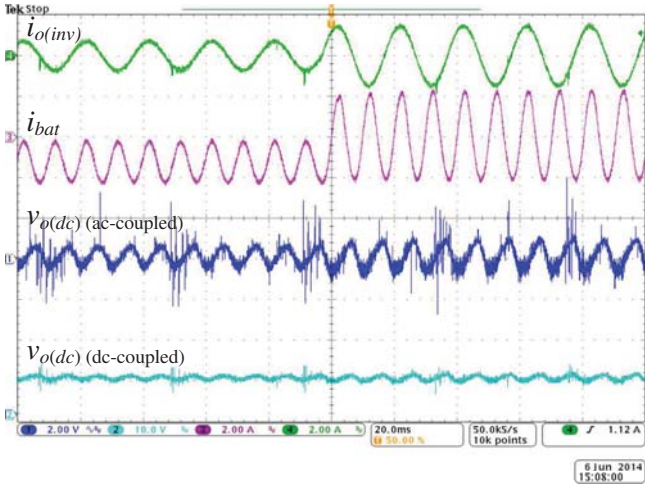

(b)

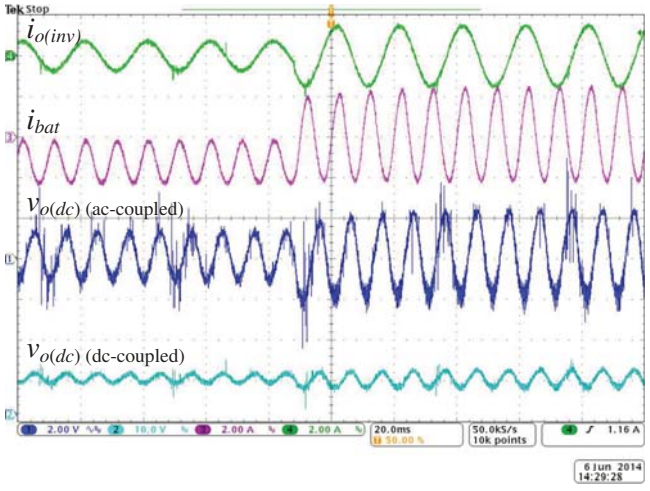

(c)

Figure 23: Dynamic converter waveforms with (a) PI only; (b) PI and load-current feed-forward; and (c) PI and virtual resistor.

This article has been accepted for publication in a future issue of this journal, but has not been fully edited. Content may change prior to final publication. Citation information: DOI 10.1109/TPEL.2014.2369573, IEEE Transactions on Power Electronics

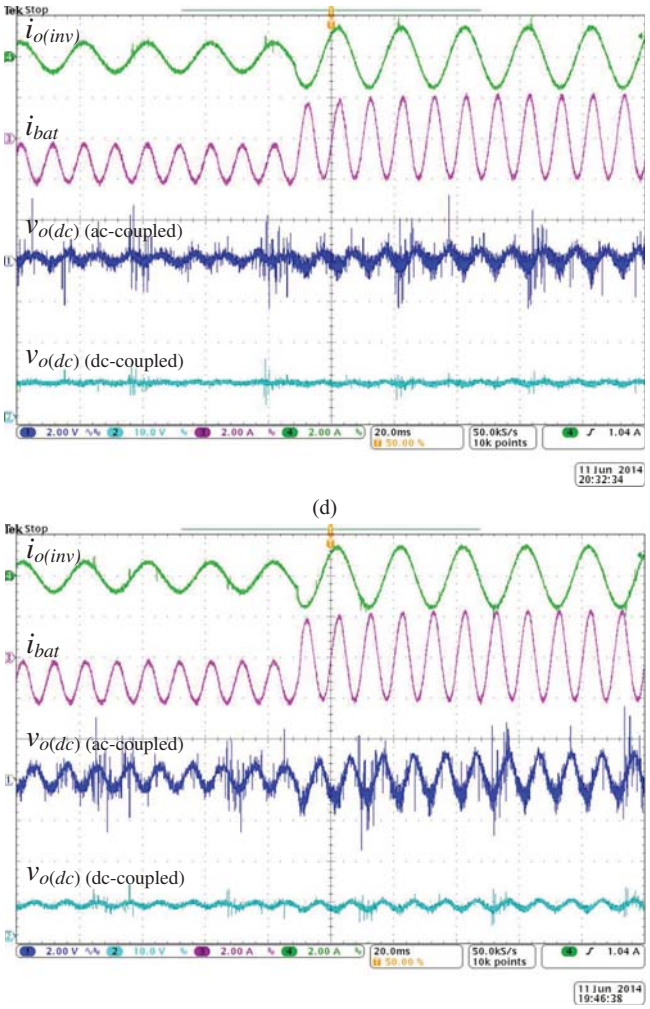

Figure 23: Dynamic converter waveforms with (d) PI and virtual capacitor; and (e) PI and virtual inductor.

This article has been accepted for publication in a future issue of this journal, but has not been fully edited. Content may change prior to final publication. Citation information: DOI 10.1109/TPEL.2014.2369573, IEEE Transactions on Power Electronics

6 Conclusion

In conclusion, four basic modes of output-impedance shaping method as can be inferred directly from the Mason's gain formula were communicated in this paper. The general idea is to design additional forward paths or feedback loops in such a way that they contribute to minimizing and maximizing the numerator and denominator of the Mason's gain formula, respectively, in order to minimize the overall converter's closed-loop output impedance. This paper has laid down the four basic modes of such approach, namely the load-current feed-forward, virtual resistor, virtual capacitor, and virtual inductor, based on which more complex impedances can be derived by combining them in ways that suit the specific needs of particular converter systems requiring output-impedance shaping, such as those renewable energy systems involving ripple-sensitive devices such as fuel cells, photovoltaic cells, and electrochemical storage devices. Today, these complex output impedances can be readily implemented by using digital controllers. In this paper, an example system based on multi-input bidirectional DAB dc-dc converter was constructed for testing their performances in shaping the energy storage branch's output impedance. It was shown that they gave rise to different degrees of output-impedance shaping capabilities. So far no conclusion is made in respect of which of these modes (or their derivatives or combinations) or design approach will give the optimum result. Their application should be considered in conjunction with the particular characteristics of the converter systems to be optimized, such as intrinsic output impedance and existing control system design.

Acknowledgment

This work was supported by the University Grants Committee of the Hong Kong Special Administrative Region, Research Grants Council, under Earmarked Research Grants PolyU 5185/11 and PolyU 5390/13.

References

[1] G. Fontes, C. Turpin, R. Saisset, T. Meynard, and S. Astier, "Interactions between fuel cells and power converters influence of current harmonics on a fuel cell stack," *IEEE Transactions on Power Electronics*, vol. 22, no. 2, pp. 670–678, March 2007

[2] R. Ferrero, M. Marracci, and B. Tellini, "Single PEM fuel cell analysis for the evaluation of current ripple effects," *IEEE Transactions on Instrumentation and Measurement*, vol. 62, no. 5, pp. 1058–1064, May 2013

[3] W. Choi, P. N. Enjeti, J. W. Howze, and G. Joung, "An experimental evaluation of the effects of ripple current generated by the power conditioning stage on a proton exchange membrane fuel cell stack," *Journal of Materials Engineering and Performance*, vol. 13, no. 3, pp. 257–264, June 2004

[4] F. Sergi, G. Brunaccini, A. Stassi, A. Di Blasi,G. Dispenza, A. S. Arico,M. Ferraro, and V. Antonucci, "PEM fuel cells analysis for grid connected applications," *International Journal of Hydrogen Energy*, vol. 36, no. 17, pp. 10908–10916, August 2011

[5] C. Liu and J. S. Lai, "Low frequency current ripple reduction technique with active control in a fuel cell power system with inverter load," *IEEE Transactions on Power Electronics*, vol. 22, no. 4, pp. 1429–1436, July 2007

[6] R. Bojoi, C. Pica,D. Roiu, and A. Tenconi, "New DC-DC converter with reduced low-frequency current ripple for fuel cell in single-phase distributed generation," *IEEE International Conference on Industrial Technology (ICIT)*, 14–17 March 2010, pp. 1213–1218

[7] Y. J. Song and P. N. Enjeti, "A high frequency link direct DC-AC converter for residential fuel cell power systems," *IEEE 35th Annual Power Electronics Specialists Conference, PESC 04*, 20–25 June 2004, pp. 4755–4761

[8] J. M. Kwon, E. H. Kim, B. H. Kwon, and K. H. Nam, "High-efficiency fuel cell power conditioning system with input current ripple reduction," *IEEE Transactions on Industrial Electronics*, vol. 56, no. 3, pp. 826–834, March 2009

[9] X. Liu, H. Li, and Z. Wang, "A fuel cell power conditioning system with low-frequency ripple-free input current using a control-oriented power pulsation decoupling strategy," *IEEE Transactions on Power Electronics*, vol. 29, no. 1, pp. 159–169, January 2014

[10] H. Qin and J. W. Kimball, "Closed-loop control of DC-DC dual-active-bridge converters driving single-phase inverters," *IEEE Transactions on Power Electronics*, vol. 29, no. 2, pp. 1006–1017, February 2014

[11] P. T. Krein, R. S. Balog, and M. Mirjafari, "Minimum energy and capacitance requirements for single-phase inverters and rectifiers using a ripple port," *IEEE Transactions on Power Electronics*, vol. 27, no. 11, pp. 4690–4698, November 2012

[12] A. C. Kyritsis, N. P. Papanikolaou,and E. C. Tatakis, "A novel parallel active filter for current pulsation smoothing on single stage grid-connected AC-PV modules," *European Conference on Power Electronics and Applications*, 2–5 September 2007, pp. 1–10

[13] J. L. Duarte, M. Hendrix, and M. G. Simoes, "Three-port bidirectional converter for hybrid fuel cell systems," *IEEE Transactions on Power Electronics*, vol. 22, no. 2, pp. 480–487, March 2007

[14] H. Tao, A. Kotsopoulos, J. L. Duarte, and M. A. M. Hendrix, "Transformer-coupled multiport ZVS bidirectional DC-DC converter with wide input range," *IEEE Transactions on Power Electronics*, vol. 23, no. 2, pp. 771–781, March 2008

[15] D. Liu and H. Li, "A ZVS bidirectional DC-DC converter for multiple energy storage elements," *IEEE Transactions on Power Electronics*, vol. 21, no. 5, pp. 1513–1517, September 2006

[16] X. Li, W. Zhang, H. Li, R. Xie, M. Chen, G. Shen, and D. Xu, "Power management unit with its control for a three-phase fuel cell power system without large electrolytic capacitors," *IEEE Transactions on Power Electronics*, vol. 26, no. 12, pp. 3766–3777, July 2011

[17] R. Redl, and N. O. Sokal, " Near-optimum dynamic regulation of DC-DC converters using feed-forward of output current and input voltage with current-mode control," *IEEE Transactions on Power Electronics*, vol. PE-1, no. 3, pp. 181–192, July 1986

[18] M. Karppanen, M. Hankaniemi, T. Suntio, and M. Sippola , "Dynamical characterization of peak-current-mode-controlled buck converter with output-current feedforward," *IEEE Transactions on Power Electronics*, vol. 22, no. 2, pp. 444–451, March 2007

[19] L. Varga, and N. Losic, "Synthesis of zero-impedance converter," *IEEE Transactions on Power Electronics*, vol. 7, no. 1, pp. 152–170, March 1992

[20] J. M. Guerrero, L. G. Vicuna, J. Matas, M. Castilla and J. Miret, "Output impedance design of parallel-connected UPS inverters with wireless loadsharing control," *IEEE Transactions on Industry Applications*, vol. 52, no. 4, pp. 1126–1135, Aug. 2005

[21] M. Liserre, A. DellAquila, and F. Blaabjerg, "Genetic algorithm-based design of the active damping for an LCL-filter three-phase active rectifier," *IEEE Transactions on Power Electronics*, vol. 19, no. 1, pp. 76–86, Jan. 2004

[22] Y. W. Li, B. Wu, N. R. Zargari, J. C. Wiseman, and D. Xu, " Damping of PWM current-source rectifier using a hybrid combination approach," *IEEE Transactions on Power Electronics*, vol. 22, no. 4, pp. 1383–1393, Jul. 2007

[23] X. Zhou, J. Fan, and A. Q. Huang, "High-frequency resonance mitigation for plug-In hybrid electric vehicles integration with a wide range of grid conditions," *IEEE Transactions on Industry Applications*, vol. 27, no. 11, pp. 4459–4471, Nov. 2012

[24] E. Twining , and D. G. Holmes , " Grid current regulation of a three-phase voltage source inverter with an LCL input filter," *IEEE Transactions on Power Electronics* , vol. 18, no. 3, pp. 888–895, May 2003

[25] W. Cai, B. Liu, S. Duan, and L. Jiang, "An active low-grequency ripple control method based on the virtual capacitor concept for BIPV systems," *IEEE Transactions on Power Electronics*, vol. 29, no. 4, pp. 1733–1745, April 2014

[26] P. A. Dahono, and D. P. Wulandari, "Low-frequency output current ripple minimization by using virtual inductor," *International Conference on Power Electronics and Drives Systems, PEDS 05*, 28 Nov.–01 Dec. 2005, pp. 822–826

[27] H. Li, F. Z. Peng, and J. S. Lawler, "A natural ZVS medium-power bidirectional DC-DC converter with minimum number of devices," *IEEE Transactions on Industry Applications*, vol. 39, no. 2, pp. 525–535, March 2003

[28] L. Cao, K. H. Loo, and Y. M. Lai, "Frequency-adaptive filtering of low-frequency harmonic current in fuel cell power conditioning systems," *IEEE Transactions on Power Electronics* (in press)

[29] N. S. Nise, *Control Systems Engineering*, sixth edition, John Wiley & Sons, 2011